






# Geophysical Research Letters<sup>®</sup>



## RESEARCH LETTER

10.1029/2023GL104092

## *Trichodesmium* Around Australia: A View From Space

Lin Qi<sup>1,2</sup> , Menghua Wang<sup>1</sup> , Chuanmin Hu<sup>3</sup> , Douglas G. Capone<sup>4</sup>, Ajit Subramaniam<sup>5</sup> , Edward J. Carpenter<sup>6</sup>, and Yuyuan Xie<sup>3</sup> 

### Key Points:

- Deep learning was applied to multi-band satellite images to detect and quantify *Trichodesmium* surface scums around Australia
- *Trichodesmium* scums were found nearly everywhere around Australia with a seasonality and a cumulative footprint exceeding 4.6 million km<sup>2</sup>
- Distribution and seasonality of *Trichodesmium* were driven by temperature, iron-rich dust and black carbon from the mainland bushfires

### Supporting Information:

Supporting Information may be found in the online version of this article.

### Correspondence to:

L. Qi,  
[Lin.Qi@noaa.gov](mailto:Lin.Qi@noaa.gov)

### Citation:

Qi, L., Wang, M., Hu, C., Capone, D. G., Subramaniam, A., Carpenter, E. J., & Xie, Y. (2023). *Trichodesmium* around Australia: A view from space. *Geophysical Research Letters*, 50, e2023GL104092. <https://doi.org/10.1029/2023GL104092>

Received 13 APR 2023  
Accepted 26 JUL 2023

### Author Contributions:

**Conceptualization:** Lin Qi  
**Data curation:** Lin Qi, Douglas G. Capone, Ajit Subramaniam, Edward J. Carpenter, Yuyuan Xie  
**Formal analysis:** Douglas G. Capone, Ajit Subramaniam  
**Funding acquisition:** Menghua Wang, Chuanmin Hu  
**Investigation:** Lin Qi, Chuanmin Hu, Douglas G. Capone, Ajit Subramaniam, Edward J. Carpenter, Yuyuan Xie  
**Methodology:** Lin Qi, Chuanmin Hu

© 2023. The Authors. *Geophysical Research Letters* published by Wiley Periodicals LLC on behalf of American Geophysical Union.

This is an open access article under the terms of the [Creative Commons Attribution License](https://creativecommons.org/licenses/by/4.0/), which permits use, distribution and reproduction in any medium, provided the original work is properly cited.

<sup>1</sup>NOAA Center for Satellite Applications and Research, College Park, MD, USA, <sup>2</sup>Global Science & Technology Inc., Greenbelt, MD, USA, <sup>3</sup>College of Marine Science, University of South Florida, St. Petersburg, FL, USA, <sup>4</sup>University of Southern California, Los Angeles, CA, USA, <sup>5</sup>Lamont Doherty Earth Observatory, Columbia University, Palisades, NY, USA, <sup>6</sup>Biology Department, Estuary & Ocean Science Center, San Francisco State University, Tiburon, CA, USA

**Abstract** The cyanobacterium *Trichodesmium* is responsible for approximately half of the ocean's nitrogen input through nitrogen fixation. Although it was first recorded near Australia in the 18th century, the knowledge of where and when large quantity of *Trichodesmium* around Australia could be found is still lacking. Here, using multi-band satellite imagery acquired between 2012 and 2021, we fill this knowledge gap through the use of deep learning, designed to recognize both the spectral shapes of individual pixels and spatial morphology of surface aggregations (scums) of *Trichodesmium*. *Trichodesmium* scums were found nearly everywhere around Australia, with a cumulative footprint (i.e., where the 10-year average density is >0.001‰) exceeding 4.6 million km<sup>2</sup>. Strong seasonality was found, with peak months between September and November. Furthermore, temperature, iron-rich dust and black carbon aerosols, with the latter being a result of frequent bushfires, play major roles in determining the spatial distributions and seasonality of *Trichodesmium*.

**Plain Language Summary** Responsible for half of the ocean's nitrogen input through nitrogen fixation, the saltwater cyanobacterium *Trichodesmium* is ubiquitous in global tropical and subtropical oceans but particularly abundant around Australia. However, although the earliest report goes back to the 18th century, the knowledge of where and when large quantities of *Trichodesmium* can be found around Australia is still incomplete. Based on satellite imagery and deep learning, we quantified relative abundance of *Trichodesmium* around Australia for the period of 2012–2021. Surface aggregations of *Trichodesmium* were found almost everywhere except the southern coast, with a cumulative footprint exceeding 4.6 million km<sup>2</sup>. Strong seasonality was found, with peak months between September and November. The spatial distributions and seasonality were found to correlate well with water temperature, iron-rich dust from Australian desert, and black carbon aerosols from frequent bushfires. With the projected ocean warming in the coming century, *Trichodesmium* may expand further south, making the cumulative footprint even larger.

## 1. Introduction

*Trichodesmium* is a filamentous cyanobacteria, with *Trichodesmium erythraeum* and *Trichodesmium thiebautii* being the most reported species in the open ocean (Carpenter & Capone, 1992). With abundant gas vesicles, *Trichodesmium* cells can often form buoyant colonies on the surface that appear yellowish or brownish, thus often called sea sawdust (Walsby, 1992). *Trichodesmium* plays a critical role in the ocean's nitrogen cycle, as it is able to fix nitrogen (N<sub>2</sub>) to ammonia (NH<sub>4</sub><sup>+</sup>) that can be used by itself and other phytoplankton (Capone et al., 1997, 2005; Carpenter & Capone, 1992). On the global scale, *Trichodesmium* can provide about 80 Tg of new nitrogen per year (Capone et al., 1997), representing ~50% of the total new nitrogen demand in oligotrophic oceans (Capone et al., 2005; Karl et al., 1997). *Trichodesmium* has been reported in oligotrophic oceans, particularly in tropical and subtropical regions where nitrate is scarce. *Trichodesmium* requires iron (Fe) to grow and fix nitrogen (Kustka et al., 2003; Rueter et al., 1992), and both laboratory and field studies showed immediate biomass increases with additional Fe supplies (Lenes et al., 2001; Tzubarri et al., 2018).

To date, despite numerous observational and modeling studies at both local and global scales (Blondeau-Patissier et al., 2018; Capone et al., 1997; Davies et al., 2020; Delmont, 2021; M. Furnas, 1992; M. J. Furnas & Carpenter, 2016; Gower et al., 2014; Hu et al., 2010; Karlusich et al., 2021; Y. W. Luo et al., 2012; L. McKinna, 2015; Monteiro et al., 2010; Qi & Hu, 2021; Subramaniam & Carpenter, 1994; Tang & Cassar, 2019; Westberry & Siegel, 2006), the global distributions of *Trichodesmium* are still unclear. Even in waters around

**Project Administration:** Menghua Wang, Chuanmin Hu  
**Resources:** Edward J. Carpenter  
**Supervision:** Menghua Wang, Chuanmin Hu  
**Visualization:** Lin Qi  
**Writing – original draft:** Lin Qi, Menghua Wang, Chuanmin Hu, Douglas G. Capone, Ajit Subramaniam, Edward J. Carpenter, Yuyuan Xie  
**Writing – review & editing:** Lin Qi, Menghua Wang, Chuanmin Hu, Douglas G. Capone, Ajit Subramaniam, Edward J. Carpenter, Yuyuan Xie

Australia, where *Trichodesmium* was first reported in the 18th century (M. Furnas, 1992), a thorough knowledge of *Trichodesmium* distributions is still lacking.

There have been long-term monitoring programs to measure *Trichodesmium* around Australia. One such program is the Australia's Integrated Marine Observing System (IMOS, <https://imos.org.au/>; Eriksen et al., 2019). However, these programs are focused on individual sampling sites. Satellite remote sensing has also been used to map *Trichodesmium* surface scums (i.e., surface layer with high concentrations of cells and/or colonies to result in elevated reflectance in the near-infrared wavelengths, see Qi et al., 2018) (see summary in Table S1 and Figure S1 in Supporting Information S1), with the assumption that surface scums can serve as a proxy to represent abundance. Yet these remote sensing studies are either case studies or focused on selected regions (e.g., the Great Barrier Reef or GBR, Blondeau-Patissier et al., 2018; L. McKinna, 2015), thus not being able to provide information on all coastal waters around Australia, especially on where and why *Trichodesmium* blooms occur regularly there.

Here, based on the Visible Infrared Imaging Radiometer Suite (VIIRS) satellite observations and a computer deep learning (DL) model, we develop monthly maps of *Trichodesmium* scum density for a 10-year period between 2012 and 2021 (see Figures S2–S6 and Table S2 for methodology in Supporting Information S1). We analyze the spatial and temporal distributions changes of *Trichodesmium* as well as possible factors leading to such distributions, including atmospheric dust, black carbon (BC) aerosols, water temperature, winds, and ocean currents. We hypothesize that dust and BC are the two primary factors in determining the spatial distributions and seasonality of *Trichodesmium* around Australia.

## 2. Data and Method

The study around Australia (8°S–40°S and 110°E–160°E, Figure 1a) was based on data collected by VIIRS, the Ocean and Land Color Instruments (OLCI), and the Hyperspectral Imager for the Coastal Ocean (HICO). VIIRS was used to develop time-series of *Trichodesmium* density maps, while limited OLCI and HICO data were used to perform spectral discrimination analysis to verify whether the observed image features were due to *Trichodesmium* or something else. Briefly, for each VIIRS image, pixels containing *Trichodesmium* were first delineated using a DL model (specifically, Res-UNet, see application of the same approach to extract *Sargassum* image features from multi-band imagery over the Atlantic Ocean in Hu et al. (2023)). The DL model relies not only on the reflectance spectral shapes of individual pixels, but also on the spatial context of each pixel, and can be re-trained to improve detection accuracy through minimizing false-positive and false-negative detections, therefore showing better performance over other index-based models (e.g., the alternative floating algae index (AFAI)-based model, Hu et al., 2023). Once *Trichodesmium* features are detected from individual images, a spectral unmixing scheme was used to determine the sub-pixel proportion of *Trichodesmium* (0%–100% within a pixel), and multiple images were used to compose monthly and annual maps. Here, the detected *Trichodesmium* image features refer to surface scums as opposed to cells or colonies suspended in water. The scums show distinctive pigment features in their reflectance spectra (Figures S2 and S3 in Supporting Information S1), indicative of active nitrogen and carbon fixation as reported in the Arabian Sea from similar scums (Capone et al., 1998). More details on this method and its validity can be found in Supporting Information S1.

To interpret the observed spatial patterns and temporal changes of *Trichodesmium*, environmental data from different data sources were downloaded and analyzed. These include: daily sea surface temperature (SST), chlorophyll-*a* (Chl-*a*) concentration, wind speed, and sea surface current velocity; monthly mean dust and BC density in the atmosphere, mixed-layer depth (MLD); all-time averages (i.e., climatology) of sea surface nutrient (nitrogen and phosphorous) concentrations. Further details on these data types can be found in Supporting Information S1.

## 3. Results and Discussion

### 3.1. *Trichodesmium* Around Australia: Where and When?

The distribution of average surface density of *Trichodesmium* between 2012 and 2021 is shown in Figure 1a, and more detailed climatological monthly and annual distributions can be found in Figures S7 and S8 in Supporting Information S1, respectively. In the study region (8°S–40°S, 110°E–160°E), *Trichodesmium* scums can be observed almost everywhere around Australia except off the southern coast between 32°S and 40°S and

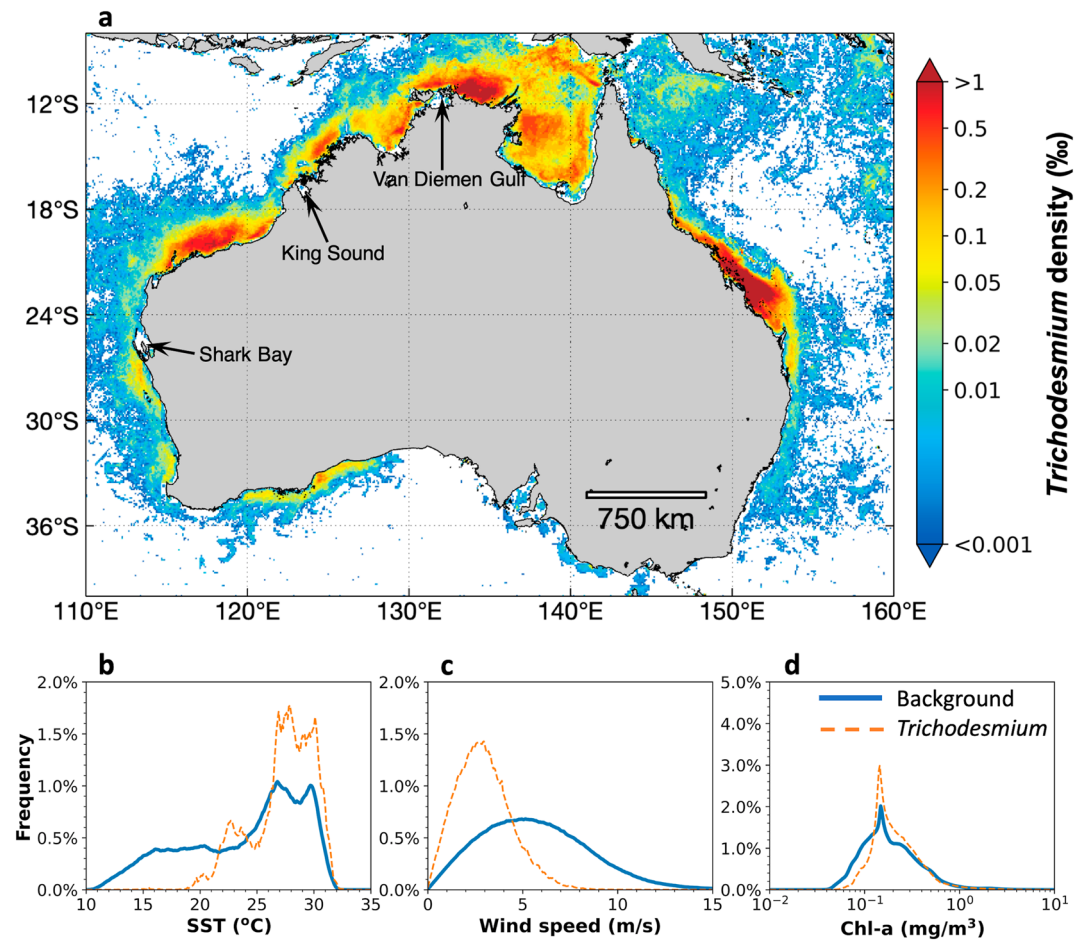


**Figure 1.** (a) Average surface cover density (in ‰) of floating *Trichodesmium* (i.e., surface scums) around Australia, based on Visible Infrared Imaging Radiometer Suite observations (2012–2021); (b–d) histograms of sea surface temperature, wind speed, and chlorophyll-*a* (Chl-*a*) concentration, respectively, corresponding to occurrence locations of floating *Trichodesmium* (red dashed lines) and their background water of *Tricho*-niche area (i.e., the cumulative footprint area, blue lines). Statistics for tropical/subtropical waters (north of 23.45°S) and temperate waters (south of 23.45°S) are presented in Figure S10 in Supporting Information S1. No *Trichodesmium* scums were found between 40°S and 44°S (including waters around Tasmania), and this area is therefore not included in the map (a). The cumulative footprint, defined as the waters with an average density of >0.001‰ in (a), is ~4.6 million km<sup>2</sup>. Climatological monthly and annual mean distributions of *Trichodesmium* are available in Supporting Information S1.

130°E–150°E. No scums were observed to the south of 40°S (not covered by the map). This is generally in agreement with the model predictions based on field observations (Davies et al., 2020). From Figure 1a, the cumulative footprint of *Trichodesmium*, defined as the waters with a climatological average surface density of >0.001‰, is approximately 4.6 million km<sup>2</sup>. This is equivalent to 60% of Australia's land area.

The distribution is uneven, with most *Trichodesmium* scums found north of ~24°S, for example, in the GBR region, Gulf of Carpentaria, and Arafura Sea. In contrast, in the region south of ~24°S, *Trichodesmium* density is much lower, and no *Trichodesmium* scums were found in the entire 10-year period for the southeast region bounded by 32°S–40°S and 130°E–150°E. Furthermore, the density generally decreased with increasing distance from shore, suggesting possibly land-based nutrient inputs. These spatial patterns are relatively stable from year to year (Figure S8 in Supporting Information S1). The density in this cumulative map is mostly <1‰, suggesting that the appearance of *Trichodesmium* scums is sporadic. This is particularly true for the relatively shallow and dynamic coastal waters such as the Van Diemen Gulf, King Sound, and Shark Bay (Figure 1a). Even though *Trichodesmium* has been reported in these waters, *Trichodesmium* scums were formed much less frequently than in the adjacent, more offshore waters. This is possibly due to the more dynamic water column mixing in these shallow environments (Blondeau-Patissier et al., 2017).

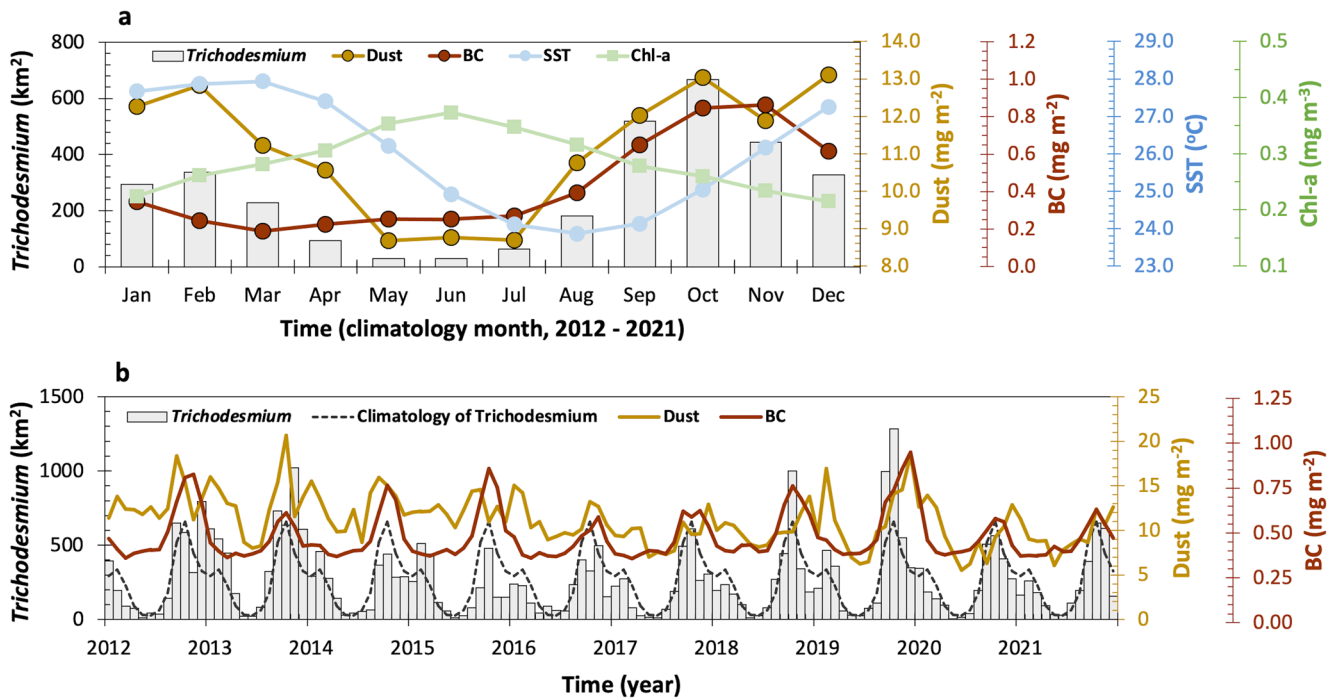


**Figure 2.** Seasonality (a) and monthly time series (b) of *Trichodesmium* areal coverage between 2012 and 2021. In panel (a), dust, black carbon (BC) aerosols, sea surface temperature, and Chl-*a* derived from the *Tricho*-niche area (i.e., total cumulative footprint area, Figure 1a) are presented. In panel (b), monthly *Trichodesmium* and its corresponding dust and BC from the *Tricho*-niche area are shown, overlaid with the monthly climatological *Trichodesmium*.

Similar to the uneven spatial distributions, *Trichodesmium* was not found equally in all months, but showed a clear seasonality (Figure 2a, Figure S7, and Table S3 in Supporting Information S1) and interannual variability (Figures S8 and S9 in Supporting Information S1) regardless of whether tropical/subtropical and temperate waters were considered together or separately (Figure S10 in Supporting Information S1). The maximum and minimum bloom sizes were found in September–November and May–July, respectively, with a maximum/minimum ratio of about 5. The peak months of *Trichodesmium* blooms can vary slightly from year to year (Figure 2b and Table S3 in Supporting Information S1). For example, in 2014 and 2015, the peak month was February, but there was also a secondary peak in October. In contrast, the months with the minimum bloom size were more stable in different years, mostly between May and July.

### 3.2. *Trichodesmium* Around Australia: Why?

As per literature and findings prior to this study, *Trichodesmium* scums were not found uniformly in different environments but predominantly in waters within certain temperature and Chl-*a* ranges and under relatively calm conditions (Figures 1b–1d) regardless of whether the entire study region was split into tropical/subtropical (north of 23.45°S) and temperate waters (south of 23.45°S) (Figure S10 in Supporting Information S1). Here, the 10-year cumulative *Trichodesmium* footprint was used as the *Tricho*-niche area, serving as the background water where *Trichodesmium* scums could be found (i.e., average 10-year density of *Trichodesmium* >0.001‰ in Figure 1a). SST from *Tricho*-niche waters covered a relatively wide range of 10–32°C, but image pixels containing *Trichodesmium* scums were found in a narrower range of 20–32°C, with the most optimal temperature around 27°C. This temperature range has been reported as the optimal range for *Trichodesmium* growth in the laboratory (Breitbarth et al., 2007). Wind speeds over the *Tricho*-niche waters ranged from 0 to 15 m s<sup>-1</sup>, but most image pixels containing *Trichodesmium* scums were found at <~6 m s<sup>-1</sup> (peak frequency ~3.5 m s<sup>-1</sup>), a result consistent with the findings by Blondeau-Patissier et al. (2018). Likewise, of a relatively wide range of Chl-*a* found from the *Tricho*-niche waters (0.04–2 mg m<sup>-3</sup>), *Trichodesmium* pixels were found with a narrower Chl-*a* range of 0.07–2 mg m<sup>-3</sup> and a peak value of ~0.2 mg m<sup>-3</sup> (Figure 1d). This suggests that, although *Trichodesmium* prefers oligotrophic waters (Capone et al., 1997), it may not survive if the water is extremely poor in nutrients (i.e., Chl-*a* < 0.07 mg m<sup>-3</sup>). Above this Chl-*a* concentration, *Trichodesmium* may reproduce well and fertilize other

phytoplankton through nitrogen fixation. Here, Chl-*a* is used in a relative sense because of the likely large uncertainties of satellite data products over optically complex coastal waters (Cannizzaro et al., 2013; IOCCG, 2019).

From these results, both the spatial distribution patterns and seasonality of *Trichodesmium* appear to be explained well by the overall nutrient regime and environmental settings around Australia, with some factors playing more important roles than others (Figure 3).

Surrounded by the Indian Ocean and the South Pacific Ocean and being far away from other continents, Australia is the smallest continent on Earth, making it isolated from remote nutrient sources. Thus, local nutrient sources must play a major role in determining the spatial distributions and seasonality of *Trichodesmium*. While average surface nitrate concentration ( $<0.6 \mu\text{mol/kg}$ , Voss et al., 2013) suggests oligotrophic conditions, the sea surface nitrate to phosphate ratio (N:P) in surface waters around Australia is  $\sim 2:1$  (Figure 3a), much lower than the Redfield ratio of 16:1 required for phytoplankton growth (Lenton & Watson, 2000). Although phosphorus is also a critical nutrient required by *Trichodesmium* (Hynes et al., 2009; Sohm et al., 2008), such a low N/P ratio and oligotrophic condition, together with the optimal temperature range and light availability, provide favorable conditions for *Trichodesmium* to grow as long as another micronutrient, iron, is supplied by certain sources such as riverine input or atmospheric deposition.

With no large river discharging waters to the ocean as compared to many other continents (McMahon & Finlayson, 2003) and with relatively narrow river plume width as compared with shelf width (Sharples et al., 2017), riverine influence on the *Trichodesmium* distributions is expected to be restricted to nearshore waters. Furthermore, compared with other parts of Australia, riverine inputs of dissolved inorganic nitrogen and dissolved inorganic phosphorus to the northwest coast of Australia are lower (Sharples et al., 2017). Thus, the relatively high density of *Trichodesmium* along that part of coast must be driven by factors other than riverine discharge. In the south, riverine flows to the coast are greater in the austral winter (June, July, and August) than in the austral summer (December, January, and February), but there is virtually no *Trichodesmium* found in the south. On the east coast, there are relatively large rivers that discharge to the north and north-east. However, the river flows are extremely seasonal and have high interannual variability, dominated by large flood events in the wet season (October to May in the north) (Warfe et al., 2011). The seasonality of *Trichodesmium* in these waters (Figure S7 in Supporting Information S1) is out of phase of river flow. Therefore, riverine inputs of local nutrients may be ruled out as being a major factor influencing the large-scale distributions of *Trichodesmium*.

The local nutrient sources appear to be from dust (Figure 3b) and BC (Figure 3c). With many large deserts on the Australian continent ( $\sim 18\%$  of being permanent deserts and another  $\sim 35\%$  being episodic deserts, Geoscience Australia, 2023), Australia is a major source of dust, with mean dust pathways from the continent to northwest and southeast (De Deckker, 2019) (Figure 3b). Likewise, bushfires or biomass burning are widespread in the northern and southeastern Australia every year because of the dry climate, resulting in high concentrations of BC aerosols with similar southeast-northwest orientation (Figure 3c). Aerosol deposition is an important source of nutrient and iron input to the ocean (Jickells & Moore, 2015; Polyviou et al., 2018; Schulz et al., 2012), and both dust and BC can supply nutrients in the form of C, N, P, and iron to the ocean (Mallet et al., 2017), stimulating growth of *Trichodesmium* and other phytoplankton (Sohm et al., 2011). For example, on the West Florida Shelf, following a Saharan dust event, total dissolved iron concentrations were found to increase by 30–100 folds from the background levels, with *Trichodesmium* concentrations increased by 100 folds (Lenes et al., 2001). In the GBR region, pigment concentration of phytoplankton (likely *Trichodesmium* or other cyanobacteria) was found to increase by 1.5–2 folds after a dust storm event in October 2002 (Shaw et al., 2008). Furthermore, biomass burning may substantially enhance the solubility of mineral dust around Australia, where the soluble iron can be up to  $\sim 12\%$  in the mixed aerosols (Winton et al., 2016). The soluble iron supplies from the atmosphere may help stimulate *Trichodesmium* growth in the oligotrophic waters around Australia.

The distributions of dust and BC do not always correlate with the *Trichodesmium* patterns found in Figure 1a. For example, off southeast Australia, both dust and BC concentrations appear relatively high, yet there is little or no *Trichodesmium* found. Such a disparity may be explained by the strong ocean currents off southeast Australia ( $>0.5 \text{ m s}^{-1}$ , Figure 3d), which can prevent *Trichodesmium* accumulation on the surface and may also impede *Trichodesmium* growth in the water column. In contrast, in similar latitude but off southwest Australia, although wind and SST are similar to those off southeast Australia (Figures 3e and 3f), small amount of *Trichodesmium* scums can still be found due possibly to weaker currents.

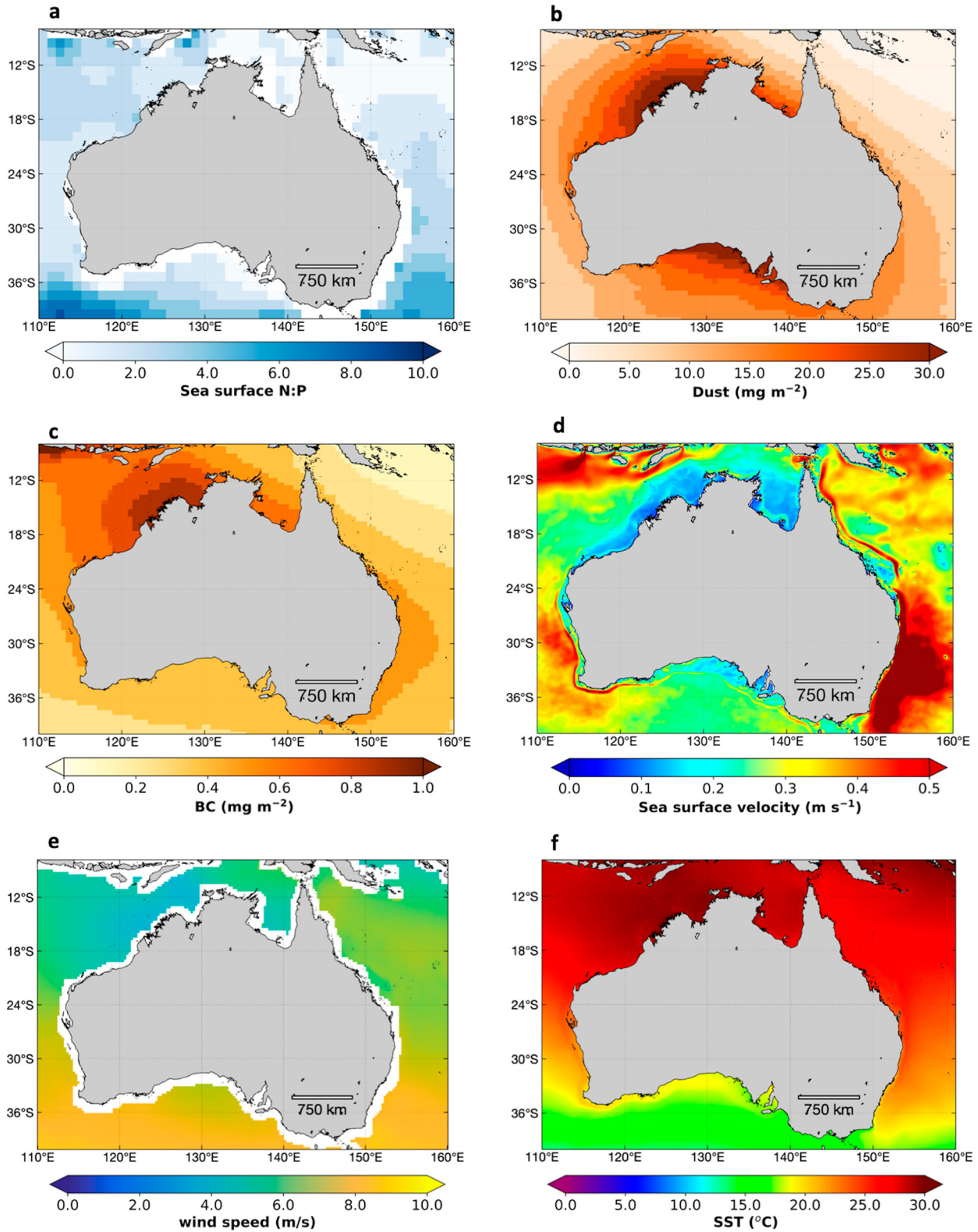


**Figure 3.** Environmental factors that are relevant to *Trichodesmium* around Australia for (a) surface water nitrate (N) to phosphorus (P) ratio (data source: WOA18), (b) and (c) mean dust and black carbon aerosol concentrations in the atmosphere between 2012 and 2021 (source: M2TINXAER model), (d) mean surface water velocity during the same period (source: Hybrid Coordinate Ocean Model), (e) and (f) mean wind speed and sea surface temperature during the same period.

In addition to influencing the spatial distributions, dust and BC appear to play an important role in driving the *Trichodesmium* seasonality as well, as all three variables are in phase (Figure 2a) with peak months of September–November and minimum months of May–July. A multi-variate correlation analysis showed strong and statistically significant correlation between *Trichodesmium* and the combined variables of BC and dust (Figure S11 in Supporting Information S1), and the regression coefficients for BC and dust are both positive, suggesting their positive influence on *Trichodesmium* growth. Such a high correlation was also found in most high-density locations (Figure S11c in Supporting Information S1). The question is whether this is simply a coincidence as opposed to causality. Because other phytoplankton (through Chl-*a*) shows the opposite phase from dust and BC (i.e., peak Chl-*a* is found between May and July, Figure 2a) and because iron-rich dust and BC are known to stimulate *Trichodesmium* growth, the latter appears to be a logical inference. In particular, the smaller size of the *Tricho*-niche water area between January and March, when dust concentration is nearly as high as that in September–November, may also be explained by the iron mechanism. This is because although dust may contain a greater amount of Fe, most of the Fe in dust aerosols is insoluble and cannot be utilized by phytoplankton (Winton et al., 2016). In contrast, BC contains a higher proportion of soluble Fe, and what's more important is that BC from biomass burning can enhance dusty mineral solubility (Hamilton et al., 2020; Hand et al., 2004; C. Luo et al., 2005; Winton et al., 2016). Thus, the relatively lower BC between January and March may be a reason to explain the lower *Trichodesmium* amount.

The opposite phase between Chl-*a* and dust/BC is perhaps the strongest reason to support the hypothesis that dust and BC can collectively control the seasonality of *Trichodesmium*. From long-term in situ measurements, phytoplankton communities around Australia are dominated by diatoms and dinoflagellates (Eriksen et al., 2019), which are driven by different environmental factors. For example, as in other subtropical oceans such as the Gulf of Mexico (GOM, Muller-Karger et al., 2015) and the South China Sea (SCS, Ji et al., 2018), non-*Trichodesmium* phytoplankton (and their associated Chl-*a*) around Australia may grow fast from nutrient enrichment due to deeper mixing in May–July induced by high winds (Figure S12 in Supporting Information S1). However, because waters around Australia are limited in Fe (Zehr & Capone, 2020), without Fe inputs from the atmosphere, the enhanced nutrients from deep waters would benefit diatoms and dinoflagellates as opposed to *Trichodesmium*. In contrast, *Trichodesmium* may benefit more than diatoms and dinoflagellates with Fe inputs from the atmosphere.

Similar to other cyanobacteria (Paerl & Huisman, 2008) and macroalgae (Qi et al., 2022), *Trichodesmium* also prefers a certain temperature range for optimal growth (Figure 1b), which may explain the overall low abundance in the south than in the north (Figures 1a and 3f). However, temperature may play a less important role in controlling the seasonality of *Trichodesmium* (Figure 2a) because the annual variation of mean SST is 24–28°C, optimal for *Trichodesmium* growth.

The collective role of dust and BC in controlling both spatial distributions (Figure 1a) and seasonality of *Trichodesmium* (Figure 2a) is also reflected in the 10-year monthly time series (Figure 2b). With no significant trend (Mann-Kendall test,  $p = 0.72$ , Hussain & Mahmud, 2019), inter-annual variations are observed in all three variables, yet a multi-variant regression analysis indicates statistically significant correlation ( $R = 0.70$ ,  $p < 0.01$ ) between *Trichodesmium* and combined dust and BC (Figure S11b in Supporting Information S1). In contrast, large-scale climate events such as El Niño and La Niña do not appear to affect the inter-annual changes in *Trichodesmium* of either tropical/subtropical waters or temperate waters, as indicated by the lack of correlation between them (Figure S13 in Supporting Information S1).

Overall, while temperature is an important factor to determine where and when *Trichodesmium* can grow, dust and BC appear to be the other two major factors to drive both spatial and temporal variations of *Trichodesmium* around Australia.

### 3.3. Impacts of Episodic Events

The dominant roles of dust and BC, as argued above, are supported by episodic events, such as the 2019–2020 bushfire event. This event, from June 2019 to March 2020, is one of the most extensive and long-lasting fires in recent years (Ward et al., 2020). It burned ~46 million acres of land covering forests, farms, and buildings, leading to mortality of 173 people and >1 billion animals (Borchers Arriagada et al., 2020; Ward et al., 2020). About ~715 million tons of CO<sub>2</sub> (195 Tg C) were released into the atmosphere during the fire period (van der Velde et al., 2021), together with nitrogen, phosphorus, and iron depositions into the ocean. The event resulted

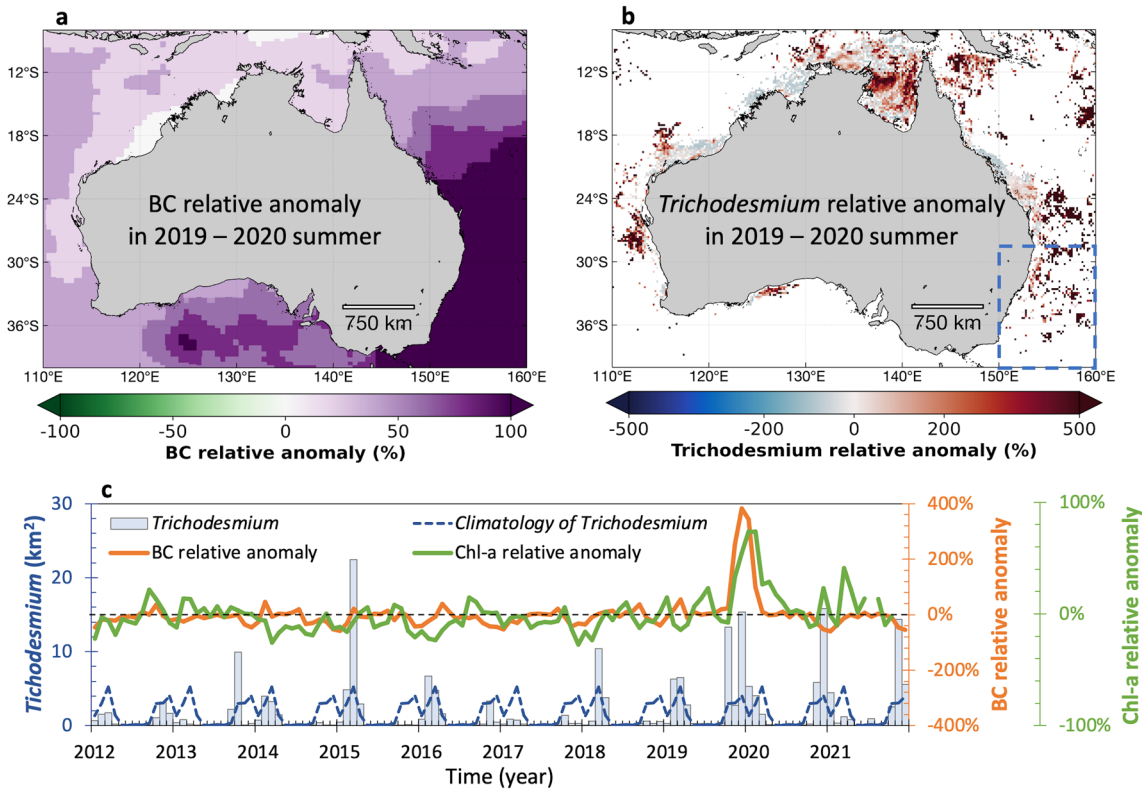


**Figure 4.** Possible influence of the 2019–2020 Australia bushfire on *Trichodesmium* and Chl-*a* for (a) relative anomaly of black carbon (BC) during the 2019–2020 austral summer season (September 2019–February 2020), (b) relative anomaly of *Trichodesmium* density for the same period, and (c) monthly time series of *Trichodesmium* coverage, relative anomaly of BC, and relative anomaly of Chl-*a* from waters off southeast Australia (blue dashed rectangle in panel (b)). Monthly climatological values of *Trichodesmium* coverage in this region are shown with a dotted dark blue line.

in significantly higher BC around most of Australia, and particularly to the southeast of Australia during the austral summer of 2019–2020 (Figure 4a) as emissions of BC were not uniform (Tang et al., 2021). If the dust/BC hypothesis was true, there would be increased *Trichodesmium* in this region. Indeed, increased *Trichodesmium* was found in this otherwise *Tricho*-poor region (Figure 4b). In other regions where *Trichodesmium* is usually high, increased *Trichodesmium* was also found. For waters off southeast Australia (blue rectangular box in Figure 4b), time-series analysis shows that the timing of the 2019–2020 *Trichodesmium* bloom event and increased Chl-*a* appeared synchronized with the positive BC anomaly (Figure 4c), suggesting a possible causality. In contrast, water temperature and MLD in this region did not show such a correspondence (Figure S14 in Supporting Information S1). In this region, higher-than-usual *Trichodesmium* in this *Tricho*-poor region in three consecutive years after the 2019–2020 bushfire event was abnormal. Using a Mann-Kendal test, no trend in *Trichodesmium* areal coverage was found for the period of 2012–2018 before the bushfire event, yet the increasing trend was statistically significant ( $p < 0.05$ ) when the post-fire years of 2019–2021 were included. To our knowledge, although there are no field data available to explain this pattern, these preliminary results suggest that iron recycling from the ash deposition could be a possible reason. However, this does not necessarily suggest that iron enrichment from bushfire events is the only possible cause of *Trichodesmium* anomalies. For example, in March 2015, an all-time high *Trichodesmium* areal coverage was found, yet there was no positive BC anomaly. The exact reason causing the March 2015 anomaly remains to be investigated.

#### 4. Concluding Remarks

Although recurrent *Trichodesmium* blooms around Australia are well known, especially in the GBR region, the knowledge of where and when blooms occurred has been incomplete until now. The improved knowledge is attributed to the synoptic and frequent satellite measurements to extract *Tricho*-specific signals using a DL technique. These observations fill the knowledge gap for previously undocumented areas along the east, west, and



southern coastlines, suggesting a broader input into the nitrogen cycle of these waters than previously appreciated. Such a knowledge paves the pathway toward the understanding of why *Trichodesmium* around most of Australia is abundant and why strong seasonality is found. For example, while the lack of *Trichodesmium* off southern Australia could be explained by low water temperature, dust and BC aerosols appear to be the other major factors controlling both the spatial distributions and seasonality of *Trichodesmium*, as they collectively serve as a major iron source to stimulate *Trichodesmium* growth. However, much remains to be done to have a better understanding of *Trichodesmium* dynamics around Australia. For example, other than dust and BC aerosols, are there any other iron inputs from ocean circulation or upwelling? With the detailed *Trichodesmium* maps made available through this study, analysis of ocean circulation through hydrodynamic modeling and incorporation of more observational data could help address this question in the near future.

Climate change is a globally pervasive process and Australian coastal waters are not immune to its influences. Upper ocean warming and stratification and acidification are ongoing (Hutchins & Fu, 2017), as well as processes in the terrestrial realm that affect coastal waters such as desertification, changes in coastal runoff and wildfires expansion, in both time and space (Hoegh-Guldberg et al., 2014). How these factors will affect *Trichodesmium* populations (and other diazotrophs) is an area of ongoing research (e.g., Fu et al., 2014), where the findings presented here may serve as the baseline to understand future changes. For example, declining wind stress and increasing SST have been shown in the south and southeast regions of Australia, with the Tasman Sea being the fastest warming region (Duran et al., 2020). Although minimal *Trichodesmium* was found in these regions from the current study, should such wind and SST trends continue in the future, increased *Trichodesmium* would be a consequence, and, likewise, expansion of *Trichodesmium* to higher latitudes could also occur (Breitbarth et al., 2007). With the continuity missions of VIIRS and other satellite missions such as the hyperspectral Plankton, Aerosol, Cloud, ocean Ecosystem (PACE) (<https://pace.gsfc.nasa.gov>), we expect to extend the data record to future years to understand how *Trichodesmium* around Australia responds to environmental conditions under a changing climate.

## Data Availability Statement

The processed data used in this study can be accessed through Mendeley Data: Qi (2023).

## Acknowledgments

This work was supported by the Joint Polar Satellite System (JPSS)/NOAA program for ocean color calibration and validation (ST13301CQ0050/1332K-P22FNEED004), by the U.S. NASA (80NSSC20M0264, 80NSSC21K0422, 80NSSC21K0439), and by the LDEO Climate and Life fellowship. We thank Dr. Barbara Robson of the Australian Institute of Marine Science for her assistance in interpreting the factors supporting *Trichodesmium* blooms around Australia. We are deeply grateful to the two anonymous reviewers who provided extremely detailed comments and suggestions to improve the presentation of this work. The scientific results and conclusions, as well as any views or opinions expressed herein, are those of the author(s) and do not necessarily reflect those of NOAA or the Department of Commerce.

## References

- Blondeau-Patissier, D., Brando, V. E., Lønborg, C., Leahy, S. M., & Dekker, A. G. (2018). Phenology of *Trichodesmium* spp. blooms in the great barrier reef lagoon, Australia, from the ESA-MERIS 10-year mission. *PLoS One*, 13(12), e0208010. <https://doi.org/10.1371/journal.pone.0208010>
- Blondeau-Patissier, D., Schroeder, T., Clementson, L. A., Brando, V. E., Purcell, D., Ford, P., et al. (2017). Bio-optical properties of two neighboring coastal regions of tropical northern Australia: The Van Diemen Gulf and Darwin Harbour. *Frontiers in Marine Science*, 4, 114. <https://doi.org/10.3389/fmars.2017.00114>
- Borchers Arriagada, N., Palmer, A. J., Bowman, D. M., Morgan, G. G., Jalaludin, B. B., & Johnston, F. H. (2020). Unprecedented smoke-related health burden associated with the 2019–20 bushfires in eastern Australia. *Medical Journal of Australia*, 213(6), 282–283. <https://doi.org/10.5694/mja2.50545>
- Breitbarth, E., Oschlies, A., & LaRoche, J. (2007). Physiological constraints on the global distribution of *Trichodesmium*—Effect of temperature on diazotrophy. *Biogeosciences*, 4(1), 53–61. <https://doi.org/10.5194/bg-4-53-2007>
- Cannizzaro, J., Hu, C., Carder, K. L., Kelble, C. R., Melo, N., Johns, E. M., et al. (2013). On the accuracy of SeaWiFS ocean color data products on the West Florida Shelf. *Journal of Coastal Research*, 29(6), 1257–1272. <https://doi.org/10.2112/JCOASTRES-D-12-00223.1>
- Capone, D. G., Burns, J. A., Montoya, J. P., Subramaniam, A., Mahaffey, C., Gunderson, T., et al. (2005). Nitrogen fixation by *Trichodesmium* spp.: An important source of new nitrogen to the tropical and subtropical North Atlantic Ocean. *Global Biogeochemical Cycles*, 19(2), GB2024. <https://doi.org/10.1029/2004GB002331>
- Capone, D. G., Subramaniam, A., Montoya, J. P., Voss, M., Humborg, C., Johansen, A. M., et al. (1998). An extensive bloom of the N<sub>2</sub> fixing cyanobacterium *Trichodesmium* in the Eastern Arabian Sea. *Marine Ecology Progress Series*, 172, 281–292. <https://doi.org/10.3354/meps172281>
- Capone, D. G., Zehr, J. P., Paerl, H. W., Bergman, B., & Carpenter, E. J. (1997). *Trichodesmium*, a globally significant marine cyanobacterium. *Science*, 276(5316), 1221–1229. <https://doi.org/10.1126/science.276.5316.1221>
- Carpenter, E. J., & Capone, D. G. (1992). Nitrogen fixation in *Trichodesmium* blooms. In *Marine pelagic cyanobacteria: Trichodesmium and other diazotrophs* (pp. 211–217). Springer.
- Davies, C., Eriksen, R., & Richardson, A. J. (2020). Spatial and seasonal trends in *Trichodesmium*. In A. J. E. R. M. T. H.-J. I. W. J. R. Richardson (Ed.), *State and trends of Australia's ocean report*. Integrated Marine Observing System (IMOS). <https://doi.org/10.26198/5e16abb949e81>
- De Deckker, P. (2019). An evaluation of Australia as a major source of dust. *Earth-Science Reviews*, 194, 536–567. <https://doi.org/10.1016/j.earscirev.2019.01.008>
- Delmont, T. O. (2021). Discovery of nondiazotrophic *Trichodesmium* species abundant and widespread in the open ocean. *Proceedings of the National Academy of Sciences*, 118(46), e2112355118. <https://doi.org/10.1073/pnas.2112355118>
- Duran, E. R., England, M. H., & Spence, P. (2020). Surface ocean warming around Australia driven by interannual variability and long-term trends in Southern Hemisphere westerlies. *Geophysical Research Letters*, 47(9), e2019GL086605. <https://doi.org/10.1029/2019GL086605>

- Eriksen, R. S., Davies, C. H., Bonham, P., Coman, F. E., Edgar, S., McEnully, F. R., et al. (2019). Australia's long-term plankton observations: The integrated marine observing system national reference station network. *Frontiers in Marine Science*, 6, 161. <https://doi.org/10.3389/fmars.2019.00161>
- Fu, F.-X., Yu, E., Garcia, N. S., Gale, J., Luo, Y., Webb, E. A., & Hutchins, D. A. (2014). Differing responses of marine N<sub>2</sub> fixers to warming and consequences for future diazotroph community structure. *Aquatic Microbial Ecology*, 72(1), 33–46. <https://doi.org/10.3354/ame01683>
- Furnas, M. (1992). Pelagic *Trichodesmium* (=Oscillatoria) in the great barrier reef region. In *Marine pelagic cyanobacteria: Trichodesmium and other Diazotrophs* (pp. 265–272). Springer.
- Furnas, M. J., & Carpenter, E. J. (2016). Primary production in the tropical continental shelf seas bordering northern Australia. *Continental Shelf Research*, 129, 33–48. <https://doi.org/10.1016/j.csr.2016.06.006>
- Geoscience Australia. (2023). Areas of Australian and territory deserts. Retrieved from <https://www.ga.gov.au/scientific-topics/national-location-information/landforms/deserts>
- Gower, J., King, S., & Young, E. (2014). Global remote sensing of *Trichodesmium*. *International Journal of Remote Sensing*, 35(14), 5459–5466. <https://doi.org/10.1080/01431161.2014.926422>
- Hamilton, D. S., Scanza, R. A., Rathod, S. D., Bond, T. C., Kok, J. F., Li, L., et al. (2020). Recent (1980 to 2015) trends and variability in daily-to-interannual soluble iron deposition from dust, fire, and anthropogenic sources. *Geophysical Research Letters*, 47(17), e2020GL089688. <https://doi.org/10.1029/2020GL089688>
- Hand, J. L., Mahowald, N. M., Chen, Y., Siefert, R. L., Luo, C., Subramaniam, A., et al. (2004). Estimates of atmospheric-processed soluble iron from observations and a global mineral aerosol model: Biogeochemical implications. *Journal of Geophysical Research*, 109(D17), D17205. <https://doi.org/10.1029/2004JD004574>
- Hoegh-Guldberg, O., Cai, R., Poloczanska, E. S., Brewer, P. G., Sundby, S., Hilmi, K., et al. (2014). The Ocean. In V. R. Barros, C. B. Field, D. J. Dokken, M. D. Mastrandrea, K. J. Mach, T. E. Bilir, et al. (Eds.), *Climate change 2014: Impacts, adaptation, and vulnerability. Part B: Regional aspects. Contribution of working group II to the fifth assessment report of the intergovernmental panel on climate change* (pp. 1655–1731). Cambridge University Press.
- Hu, C., Cannizzaro, J., Carder, K. L., Muller-Karger, F. E., & Hardy, R. (2010). Remote detection of *Trichodesmium* blooms in optically complex coastal waters: Examples with MODIS full-spectral data. *Remote Sensing of Environment*, 114(9), 2048–2058. <https://doi.org/10.1016/j.rse.2010.04.011>
- Hu, C., Zhang, S., Barnes, B. B., Xie, Y., Wang, M., Cannizzaro, J. P., & English, D. C. (2023). Mapping and quantifying pelagic *Sargassum* in the Atlantic Ocean using multi-band medium-resolution satellite data and deep learning. *Remote Sensing of Environment*, 289, 113515. <https://doi.org/10.1016/j.rse.2023.113515>
- Hussain, M., & Mahmud, I. (2019). pyMannKendall: A Python package for non parametric Mann Kendall family of trend tests. *Journal of Open Source Software*, 4(39), 1556. <https://doi.org/10.21105/joss.01556>
- Hutchins, D. A., & Fu, F. (2017). Microorganisms and ocean global change. *Nature Microbiology*, 2(6), 17058. <https://doi.org/10.1038/nmicrobiol.2017.58>
- Hynes, A. M., Chappell, P. D., Dyhrman, S. T., Doney, S. C., & Webber, E. A. (2009). Cross-basin comparison of phosphorus stress and nitrogen fixation in *Trichodesmium*. *Limnology & Oceanography*, 54(5), 1438–1448. <https://doi.org/10.4319/lo.2009.54.5.1438>
- IOCCG. (2019). Uncertainties in ocean colour remote sensing. In F. Mélin (Ed.), *IOCCG report series, no. 18, international ocean colour coordinating group, Dartmouth, Canada*. <https://doi.org/10.25607/OBP-696>
- Ji, C., Zhang, Y., Cheng, Q., Tsou, J., Jiang, T., & Liang, X. S. (2018). Evaluating the impact of sea surface temperature (SST) on spatial distribution of chlorophyll-*a* concentration in the East China Sea. *International Journal of Applied Earth Observation and Geoinformation*, 68, 252–261. <https://doi.org/10.1016/j.jag.2018.01.020>
- Jickells, T., & Moore, C. M. (2015). The importance of atmospheric deposition for ocean productivity. *Annual Review of Ecology, Evolution, and Systematics*, 46(1), 481–501. <https://doi.org/10.1146/annurev-ecolsys-112414-054118>
- Karl, D. M., Letelier, R. M., Tupas, L., Dore, J. E., Christian, J. R., & Hebel, D. (1997). The role of nitrogen fixation in biogeochemical cycling in the subtropical north Pacific Ocean. *Nature*, 388(6642), 533–538. <https://doi.org/10.1038/41474>
- Karlusich, J. J. P., Pelletier, E., Lombard, F., Carsique, M., Dvorak, E., Colin, S., et al. (2021). Global distribution patterns of marine nitrogen-fixers by imaging and molecular methods. *Nature Communications*, 12(1), 4160. <https://doi.org/10.1038/s41467-021-24299-y>
- Kustka, A. B., Sañudo-Wilhelmy, S. A., Carpenter, E. J., Capone, D., Burns, J., & Sunda, W. G. (2003). Iron requirements for dinitrogen- and ammonium-supported growth in cultures of *Trichodesmium* (IMS 101): Comparison with nitrogen fixation rates and iron: Carbon ratios of field populations. *Limnology & Oceanography*, 48(5), 1869–1884. <https://doi.org/10.4319/lo.2003.48.5.1869>
- Lenes, J. M., Darrow, B. P., Cattrall, C., Heil, C. A., Callahan, M., Vargo, G. A., et al. (2001). Iron fertilization and the *Trichodesmium* response on the West Florida shelf. *Limnology & Oceanography*, 46(6), 1261–1277. <https://doi.org/10.4319/lo.2001.46.6.1261>
- Lenton, T. M., & Watson, A. J. (2000). Redfield revisited: 1. Regulation of nitrate, phosphate, and oxygen in the ocean. *Global Biogeochemical Cycles*, 14(1), 225–248. <https://doi.org/10.1029/1999gb900065>
- Luo, C., Mahowald, N. M., Meskhidze, N., Chen, Y., Siefert, R. L., Baker, A. R., & Johansen, A. M. (2005). Estimation of iron solubility from observations and a global aerosol model. *Journal of Geophysical Research*, 110(D23), D23307. <https://doi.org/10.1029/2005JD006059>
- Luo, Y.-W., Doney, S. C., Anderson, L. A., Benavides, M., Berman-Frank, I., Bode, A., et al. (2012). Database of diazotrophs in global ocean: Abundance, biomass and nitrogen fixation rates. *Earth System Science Data*, 4(1), 47–73. <https://doi.org/10.5194/essd-4-47-2012>
- Mallet, M. D., Desservettaz, M. J., Miljevic, B., Milic, A., Ristovski, Z. D., Alroe, J., et al. (2017). Biomass burning emissions in north Australia during the early dry season: An overview of the 2014 SAFIRED campaign. *Atmospheric Chemistry and Physics*, 17(22), 13681–13697. <https://doi.org/10.5194/acp-17-13681-2017>
- McKinna, L. (2015). Three decades of ocean-color remote-sensing *Trichodesmium* spp. in the World's oceans: A review. *Progress in Oceanography*, 131, 177–199. <https://doi.org/10.1016/j.pocean.2014.12.013>
- McMahon, T. A., & Finlayson, B. L. (2003). Droughts and anti-droughts: The low flow hydrology of Australian rivers. *Freshwater Biology*, 48(7), 1147–1160. <https://doi.org/10.1046/j.1365-2427.2003.01098.x>
- Monteiro, F. M., Follows, M. J., & Dutkiewicz, S. (2010). Distribution of diverse nitrogen fixers in the global ocean. *Global Biogeochemical Cycles*, 24(3), GB3017. <https://doi.org/10.1029/2009GB003731>
- Muller-Karger, F. E., Smith, J. P., Werner, S., Chen, R., Roffer, M., Liu, Y., et al. (2015). Natural variability of surface oceanographic conditions in the offshore Gulf of Mexico. *Progress in Oceanography*, 134, 54–76. <https://doi.org/10.1016/j.pocean.2014.12.007>
- Paerl, H. W., & Huisman, J. (2008). Blooms like it Hot. *Science*, 320(5872), 57–58. <https://doi.org/10.1126/science.1155398>
- Polyviou, D., Baylay, A. J., Hitchcock, A., Robidart, J., Moore, C. M., & Bibby, T. S. (2018). Desert dust as a source of iron to the globally important diazotroph *Trichodesmium*. *Frontiers in Microbiology*, 8. <https://doi.org/10.3389/fmicb.2017.02683>
- Qi, L. (2023). “*Trichodesmium* around Australia: A view from space”, V1. <https://doi.org/10.17632/f5d72t72b3.1>

- Qi, L., Hu, C., Barnes, B. B., Lapointe, B. E., Chen, Y., Xie, Y., & Wang, M. (2022). Climate and anthropogenic controls of seaweed expansions in the east China sea and yellow sea. *Geophysical Research Letters*, *49*(19), e2022GL098185. <https://doi.org/10.1029/2022GL098185>
- Qi, L., Hu, C., Mikelsons, K., Wang, M., Lance, V., Sun, S., et al. (2020). In search of floating algae and other organisms in global oceans and lakes. *Remote Sensing of Environment*, *239*, 111659. <https://doi.org/10.1016/j.rse.2020.111659>
- Qi, L., Hu, C., Visser, P. M., & Ma, R. (2018). Diurnal changes of cyanobacteria blooms in Taihu Lake as derived from GOCI observations. *Limnology & Oceanography*, *63*(4), 1711–1726. <https://doi.org/10.1002/lno.10802>
- Rueter, J. G., Hutchins, D. A., Smith, R. W., & Unsworth, N. L. (1992). Iron nutrition of *Trichodesmium*. In *Marine pelagic cyanobacteria: Trichodesmium and other diazotrophs* (pp. 289–306). Springer.
- Schulz, M., Prospero, J. M., Baker, A. R., Dentener, F., Ickes, L., Liss, P. S., et al. (2012). Atmospheric transport and deposition of mineral dust to the ocean: Implications for research needs. *Environmental Science & Technology*, *46*(19), 10390–10404. <https://doi.org/10.1021/es300073u>
- Sharples, J., Middelburg, J. J., Fennel, K., & Jickells, T. D. (2017). What proportion of riverine nutrients reaches the open ocean? *Global Biogeochemical Cycles*, *31*(1), 39–58. <https://doi.org/10.1002/2016gb005483>
- Shaw, E. C., Gabric, A. J., & McTainsh, G. H. (2008). Impacts of aeolian dust deposition on phytoplankton dynamics in Queensland coastal waters. *Marine and Freshwater Research*, *59*(11), 951–962. <https://doi.org/10.1071/MF08087>
- Sohm, J. A., Mahaffey, C., & Capone, D. G. (2008). Assessment of relative phosphorus limitation of *Trichodesmium* spp. in the north Pacific, north Atlantic, and the north coast of Australia. *Limnology & Oceanography*, *53*(6), 2495–2502. <https://doi.org/10.4319/lno.2008.53.6.2495>
- Sohm, J. A., Webb, E. A., & Capone, D. G. (2011). Emerging patterns of marine nitrogen fixation. *Nature Reviews Microbiology*, *9*(7), 499–508. <https://doi.org/10.1038/nrmicro2594>
- Subramaniam, A., & Carpenter, E. J. (1994). An empirically derived protocol for the detection of blooms of the marine cyanobacterium *Trichodesmium* using CZCS imagery. *International Journal of Remote Sensing*, *15*(8), 1559–1569. <https://doi.org/10.1080/01431169408954191>
- Tang, W., & Cassar, N. (2019). Data-driven modeling of the distribution of diazotrophs in the global ocean. *Geophysical Research Letters*, *46*(21), 12258–12269. <https://doi.org/10.1029/2019GL084376>
- Tang, W., Lloret, J., Weis, J., Perron, M. M. G., Basart, S., Li, Z., et al. (2021). Widespread phytoplankton blooms triggered by 2019–2020 Australian wildfires. *Nature*, *597*(7876), 370–375. <https://doi.org/10.1038/s41586-021-03805-8>
- Tzubarí, Y., Magnezi, L., Be'er, A., & Berman-Frank, I. (2018). Iron and phosphorus deprivation induce sociality in the marine bloom-forming cyanobacterium *Trichodesmium*. *The ISME Journal*, *12*(7), 1682–1693. <https://doi.org/10.1038/s41396-018-0073-5>
- van der Velde, I. R., van der Werf, G. R., Houweling, S., Maasakkers, J. D., Borsdorff, T., Landgraf, J., et al. (2021). Vast CO<sub>2</sub> release from Australian fires in 2019–2020 constrained by satellite. *Nature*, *597*(7876), 366–369. <https://doi.org/10.1038/s41586-021-03712-y>
- Voss, M., Bange, H. W., Dippner, J. W., Middelburg, J. J., Montoya, J. P., & Ward, B. (2013). The marine nitrogen cycle: Recent discoveries, uncertainties and the potential relevance of climate change. *Philosophical transactions of the Royal Society of London. Series B, Biological sciences*, *368*(1621), 20130121. <https://doi.org/10.1098/rstb.2013.0121>
- Walsby, A. (1992). The gas vesicles and buoyancy of *Trichodesmium*. In *Marine pelagic cyanobacteria: Trichodesmium and other diazotrophs* (pp. 141–161). Springer.
- Ward, M., Tulloch, A. I. T., Radford, J. Q., Williams, B. A., Reside, A. E., Macdonald, S. L., et al. (2020). Impact of 2019–2020 mega-fires on Australian fauna habitat. *Nature Ecology & Evolution*, *4*(10), 1321–1326. <https://doi.org/10.1038/s41559-020-1251-1>
- Warfe, D. M., Pettit, N. E., Davies, P. M., Pusey, B. J., Hamilton, S., Kennard, M. J., et al. (2011). The ‘wet–dry’ in the wet–dry tropics drives river ecosystem structure and processes in northern Australia. *Freshwater Biology*, *56*(11), 2169–2195. <https://doi.org/10.1111/j.1365-2427.2011.02660.x>
- Westberry, T. K., & Siegel, D. A. (2006). Spatial and temporal distribution of *Trichodesmium* blooms in the world's oceans. *Global Biogeochemical Cycles*, *20*(4), GB4016. <https://doi.org/10.1029/2005gb002673>
- Winton, V. H. L., Edwards, R., Bowie, A. R., Keywood, M., Williams, A. G., Chambers, S. D., et al. (2016). Dry season aerosol iron solubility in tropical northern Australia. *Atmospheric Chemistry and Physics*, *16*(19), 12829–12848. <https://doi.org/10.5194/acp-16-12829-2016>
- Zehr, J. P., & Capone, D. G. (2020). Changing perspectives in marine nitrogen fixation. *Science*, *368*(6492), eaay9514. <https://doi.org/10.1126/science.aay9514>

## References From the Supporting Information

- Bell, P. R. F. (2021). Analysis of satellite imagery using a simple algorithm supports evidence that *Trichodesmium* supplies a significant new nitrogen load to the GBR lagoon. *Ambio*, *50*(6), 1200–1210. <https://doi.org/10.1007/s13280-020-01460-3>
- Cannizzaro, J. P., Barnes, B. B., Hu, C., Corcoran, A. A., Hubbard, K. A., Muhlbach, E., et al. (2019). Remote detection of cyanobacteria blooms in an optically shallow subtropical lagoonal estuary using MODIS data. *Remote Sensing of Environment*, *231*, 111227. <https://doi.org/10.1016/j.rse.2019.111227>
- Chatterjee, S., & Hadi, A. S. (1986). Influential observations, high leverage points, and outliers in linear regression. *Statistical Science*, *1*(3), 379–393. <https://doi.org/10.1214/ss/1177013622>
- Chin, T. M., Vazquez-Cuervo, J., & Armstrong, E. M. (2017). A multi-scale high-resolution analysis of global sea surface temperature. *Remote Sensing of Environment*, *200*, 154–169. <https://doi.org/10.1016/j.rse.2017.07.029>
- Gao, L., Wang, C., Liu, K., Chen, S., Dong, G., & Su, H. (2022). Extraction of floating raft Aquaculture areas from sentinel-1 SAR images by a Dense residual U-net model with pre-trained Resnet34 as the encoder. *Remote Sensing*, *14*(13), 3003. <https://doi.org/10.3390/rs14133003>
- Hu, C. (2022). Hyperspectral reflectance spectra of floating matters derived from Hyperspectral Imager for the Coastal Ocean (HICO) observations. *Earth System Science Data*, *14*(3), 1183–1192. <https://doi.org/10.5194/essd-14-1183-2022>
- McKinna, L. I. W. (2010). *Optical detection and quantification of Trichodesmium spp. within the Great Barrier Reef* (PhD thesis) (p. 312). James Cook University. Retrieved from <https://researchonline.jcu.edu.au/15643/>
- McKinna, L. I. W., Furnas, M. J., & Ridd, P. V. (2011). A simple, binary classification algorithm for the detection of *Trichodesmium* spp. within the Great Barrier Reef using MODIS imagery. *Limnology and Oceanography: Methods*, *9*(2), 50–66. <https://doi.org/10.4319/lom.2011.9.50>
- Mikelsons, M., & Wang, M. (2018). Interactive online maps make satellite ocean data accessible. *Eos*, *99*. <https://doi.org/10.1029/2018eo096563>
- Qi, L., & Hu, C. (2021). To what extent can *Ulva* and *Sargassum* be detected and separated in satellite imagery? *Harmful Algae*, *103*, 102001. <https://doi.org/10.1016/j.hal.2021.102001>
- Qi, L., Hu, C., Xing, Q., & Shang, S. (2016). Long-term trend of *Ulva prolifera* blooms in the western Yellow Sea. *Harmful Algae*, *58*, 35–44. <https://doi.org/10.1016/j.hal.2016.07.004>

- Roelfsema, C. M., Phinn, S. R., Dennison, W. C., Dekker, A. G., & Brando, V. E. (2006). Monitoring toxic cyanobacteria *Lyngbya majuscula* (Gomont) in Moreton Bay, Australia by integrating satellite image data and field mapping. *Harmful Algae*, 5(1), 46–56. <https://doi.org/10.1016/j.hal.2005.05.001>
- Sanderson, J. C. (1997). *Subtidal macroalgal assemblages in temperate Australian coastal waters, Australia: State of the environment technical paper series (estuaries and the sea)*. Department of the Environment. Retrieved from [https://www.researchgate.net/profile/J-Sanderson/publication/236688368\\_Subtidal\\_Macroalgal\\_Assemblages\\_in\\_Temperate\\_Australian\\_Coastal\\_Water/links/0deec532ba8270e29e000000/Subtidal-Macroalgal-Assemblages-in-Temperate-Australian-Coastal-Water.pdf](https://www.researchgate.net/profile/J-Sanderson/publication/236688368_Subtidal_Macroalgal_Assemblages_in_Temperate_Australian_Coastal_Water/links/0deec532ba8270e29e000000/Subtidal-Macroalgal-Assemblages-in-Temperate-Australian-Coastal-Water.pdf)
- Soja-Wozniak, M., Darecki, M., Wojtasiewicz, B., & Bradtke, K. (2018). Laboratory measurements of remote sensing reflectance of selected phytoplankton species from the Baltic Sea. *Oceanologia*, 60(1), 86–96. <https://doi.org/10.1016/j.oceano.2017.08.001>
- Wen, Q., Jiang, K., Wang, W., Liu, Q., Guo, Q., Li, L., & Wang, P. (2019). Automatic building extraction from Google Earth images under complex backgrounds based on deep instance segmentation network. *Sensors*, 19(2), 333. <https://doi.org/10.3390/s19020333>
- Zhang, Z., Liu, Q., & Wang, Y. (2018). Road extraction by deep residual u-net. *IEEE Geoscience and Remote Sensing Letters*, 15(5), 749–753. <https://doi.org/10.1109/lgrs.2018.2802944>

1  
2  
3  
4  
5  
6  
7  
8  
9  
10  
11  
12  
13  
14  
15  
16  
17  
18  
19  
20  
21

***Trichodesmium* around Australia: A view from space**

Lin Qi<sup>1,2\*</sup>, Menghua Wang<sup>1</sup>, Chuanmin Hu<sup>3</sup>, Douglas G. Capone<sup>4</sup>, Ajit Subramaniam<sup>5</sup>, Edward J. Carpenter<sup>6</sup>, Yuyuan Xie<sup>3</sup>

<sup>1</sup> NOAA Center for Satellite Applications and Research, College Park, MD 20740, USA

<sup>2</sup> Global Science & Technology Inc., Greenbelt, MD 20770, USA

<sup>3</sup> College of Marine Science, University of South Florida, St. Petersburg, FL 33701, USA

<sup>4</sup> University of Southern California, Los Angeles, CA 90089, USA

<sup>5</sup> Lamont Doherty Earth Observatory, Columbia University, Palisades, NY 10964, USA

<sup>6</sup> Estuary & Ocean Science Center, Biology Department, San Francisco State University, Tiburon, CA 94920, USA

\*Correspondence to: [Lin.Qi@noaa.gov](mailto:Lin.Qi@noaa.gov)

**Supplemental Materials**

## 22 **Data and Method**

23

### 24 **1. Satellite data**

25 The Visible Infrared Imaging Radiometer Suite (VIIRS) from 2012 to 2021 were processed into  
26 Rayleigh Corrected Reflectance ( $R_{rc}(\lambda)$ , dimensionless) for each spectral band at 1-km resolution.  
27 The use of  $R_{rc}(\lambda)$  data instead of fully-corrected surface reflectance in all subsequent analyses is  
28 because the latter would depend on the assumption of zero water-leaving reflectance contributions  
29 at the near-infrared (NIR) and/or shortwave infrared (SWIR) bands. Such assumption often fails  
30 over the *Trichodesmium* scums. For the entire study region of 40°N–8°S and 110°E–160°E (Fig.  
31 S1), a total of 8082 unique 6-minute granules were processed. These data were used to develop  
32 the deep-learning algorithm to extract and quantify *Trichodesmium* features, and to establish time-  
33 series maps.

34 The full-resolution Level-1B Ocean and Land Colour Instrument (OLCI) and Hyperspectral  
35 Imager for the Coastal Ocean (HICO) data were downloaded from the NASA OB.DAAC  
36 (<https://oceancolor.gsfc.nasa.gov>) and processed to generate  $R_{rc}(\lambda)$  for each spectral band at 300  
37 m and 90 m resolutions, respectively. Different from VIIRS, these data were used for spectral  
38 analysis of identified image features as both OLCI and HICO have more spectral bands than VIIRS  
39 (Qi et al., 2020; Hu, 2022).

### 40 **2. Environmental data**

41 **Daily SST.** Multi-scale Ultra-high Resolution (MUR) daily sea surface temperature (SST, °C) data  
42 (0.25° grid) for the period of 2012–2021 for the study region of 40°S–8°S and 110°E–160°E were  
43 downloaded from the NASA Jet Propulsion Laboratory  
44 (<https://podaac.jpl.nasa.gov/dataset/MUR25-JPL-L4-GLOB-v04.2>). These data products were  
45 derived from multi-sensor measurements with optimal interpolation (OI) schemes to fill the data  
46 gap (Chin et al., 2017).

47 **Daily Chl-a.** Level-3 daily chlorophyll-a (Chl-a) concentration data ( $\text{mg m}^{-3}$ , 9-km grid) for the  
48 period of 2012–2021 for the same study region were downloaded from the NASA OB.DAAC  
49 (<https://oceancolor.gsfc.nasa.gov/l3/>). These were derived from the Moderate Resolution Imaging  
50 Spectroradiometer (MODIS)/Aqua measurements using the NASA standard atmospheric  
51 correction and bio-optical inversion algorithms (see

52 [https://oceancolor.gsfc.nasa.gov/resources/atbd/chlor\\_a/](https://oceancolor.gsfc.nasa.gov/resources/atbd/chlor_a/)) after rigorous quality control. These  
53 data may be subject to large uncertainties in turbid coastal waters (Cannizzaro et al., 2013; IOCCG,  
54 2019), but they are used here as a relative index to examine changes.

55 **Daily wind speed.** Wind speed data (1° grid) at 6-hour intervals from 2012 to 2021 were  
56 downloaded from the National Center for Environmental Prediction (NCEP)/National Center for  
57 Atmospheric Research (NCAR, <https://www.weather.gov/ncep/>). Depending on the need, all the  
58 above daily data were binned to monthly data to facilitate time-series analysis.

59 **Monthly dust and black carbon.** The monthly mean column mass density of dust (dust, mg m<sup>-2</sup>)  
60 and black carbon (BC, mg m<sup>-2</sup>) (0.5° × 0.625° grid) for the period of 2012–2021 were calculated  
61 and downloaded from the Google Earth Engine (GEE) platform. These data were provided by  
62 NASA using the second Modern-Era Retrospective analysis for Research and Applications  
63 (M2T1NXAER) model ([https://disc.gsfc.nasa.gov/datasets/M2T1NXAER\\_5.12.4/summary](https://disc.gsfc.nasa.gov/datasets/M2T1NXAER_5.12.4/summary)).

64 **Sea surface velocity.** Sea surface velocity (m s<sup>-1</sup>) from the global Hybrid Coordinate Ocean Model  
65 (HYCOM, <https://www.hycom.org/hycom>) were processed and downloaded from the GEE  
66 platform.

67 **MLD.** Mixed-Layer-Depth (MLD, m) data were obtained from the Oregon State University  
68 (<http://orca.science.oregonstate.edu/1080.by.2160.monthly.hdf.mld125.hycom.php>), estimated  
69 using a global HYCOM.

70 **Sea surface nutrient.** The all-time average cumulative sea surface nutrient concentration data (1°  
71 grid), including nitrate (N) and phosphorus (P), were obtained from NOAA WOA18  
72 (<https://www.ncei.noaa.gov/access/world-ocean-atlas-2018/bin/woa18oxnu.pl>). These data were  
73 used to compute the N/P distribution for the study region.

### 74 **3. Detect and quantify *Trichodesmium* surface scums using satellite data**

75 The methodology has been detailed in Qi and Hu (2021), Qi et al. (2016; 2020), and Hu et al.  
76 (2023). For completeness, it is described here. Briefly, four steps are involved.

77 Step 1. Identify algae pixels and prepare “ground truth” images

78 This is through visual inspection, spectral analysis, manual outlining, and objective delineation.

79 For simplicity, here, the word “algae” is used for *Trichodesmium*.

80 First, VIIRS, OLCI, and HICO  $R_{rc}(\lambda)$  data were used to compose false-color Red-Green-Blue  
 81 (FRGB) images to facilitate visual inspection of image features (Qi et al., 2020). In such  
 82 composites, the spectral bands 671 nm (red), 862 nm (green), and 443 nm (blue) for VIIRS, and  
 83 674 nm (red), 865 nm (green), and 443 nm (blue) for OLCI are used. For HICO, the spectral bands  
 84 662 nm (red), 748 nm (green), and 444 nm (blue) are used. Different from the traditional RGB  
 85 composite images, the use of a NIR band as the replacement of green channel in the FRGB images  
 86 makes algae scums appear greenish due to their enhanced NIR reflectance, thus making feature  
 87 recognition straightforward. Such FRGB images at a global scale from VIIRS measurements are  
 88 actually available through the NOAA OCView online portal (Mikelsons and Wang, 2018). Figs.  
 89 S2a and S2b show examples of VIIRS AFAI and OLCI FRGB images where image features can  
 90 be visualized.

91 Once the image features are visually identified from VIIRS FRGB or AFAI images, their spectral  
 92 shapes from the corresponding OLCI image features are analyzed using the same technique as  
 93 described in Qi et al. (2020). Specifically, the difference spectra between the image feature and  
 94 nearby water pixel,  $\Delta R_{rc}(\lambda)$ , can be used for spectral diagnosis. Mathematically, we have

$$\begin{aligned}
 95 \quad \Delta R_{rc}(\lambda) &= R_{rc}^T(\lambda) - R_{rc}^W(\lambda) \\
 96 \quad &= [\chi R^A(\lambda) + (1 - \chi) R^W(\lambda)] - R^W(\lambda) \\
 97 \quad &= \chi(R^A(\lambda) - R^W(\lambda)) \\
 98 \quad &\approx \chi R^A(\lambda) \text{ [assuming } R^W(\lambda) \ll R^A(\lambda)\text{]}. \quad (1)
 \end{aligned}$$

99 Here, the subscripts “ $T$ ”, “ $W$ ”, and “ $A$ ” represent target pixel, water pixel, and pure-algae pixel,  
 100 respectively, and  $\chi$  represents the subpixel algae coverage (0%–100%) within the target pixel. The  
 101 transition from  $R_{rc}$  to surface reflectance  $R$  is because of the assumption that aerosol reflectance  
 102 over the target pixel and nearby water pixel is the same, and therefore can be subtracted off. From  
 103 Eq. (1), the spectral shape in  $\Delta R_{rc}(\lambda)$  is the same as in the endmember  $R^A(\lambda)$ , thus can be used to  
 104 infer the algae type. Fig. S2d shows some examples of  $\Delta R_{rc}(\lambda)$  derived from randomly selected  
 105 pixels with high AFAI values or in the greenish image features of Figs. S2a and S2b. To show the  
 106 spectral shapes more clearly, the spectra of the 100 randomly selected pixels are plotted in log  
 107 scale in Fig. S2e. In this figure, the changes in the spectral magnitude indicate changes in  $\chi$  of Eq.  
 108 (1), but the reflectance spectral shapes from these randomly selected pixels are nearly identical



109 (i.e., they are parallel to each other), suggesting the same type of algae. Based on the red-edge  
110 reflectance (i.e., elevated reflectance between 700 and 900 nm) as well as elevated reflectance in  
111 the green and red bands, the algae can be inferred to be *Trichodesmium*.

112 The spectral shapes of the image features can be better viewed from the HICO images because  
113 HICO is a hyperspectral sensor (Hu, 2022). Fig. S3 shows the HICO FRGB image with the spectra  
114 extracted from 100 randomly selected pixels within the image feature. The spectral “wiggling”  
115 from 400–700 nm is due to pigment absorption of Chl-a, phycourobilin (PUB), phycoerythrobilin  
116 (PEB), and phycocyanin (PC) (McKinna, 2010; Hu et al., 2010). Such reflectance spectral shapes  
117 are unique to *Trichodesmium* scums, therefore can be used to “fingerprint” them unambiguously.  
118 The reflectance magnitude at the NIR wavelengths, on the other hand, is a measure of  $\chi$  in Eq. (1)  
119 (i.e., algae density or % cover within a pixel). In this example,  $\chi$  from 2% to 20% within a HICO  
120 pixel.

121 The reflectance spectral shapes shown in Figs. S2e and S3b are characteristics of *Trichodesmium*  
122 scums due to their diagnostic pigments. From these spectral shapes, the possibility of other algae  
123 scums (e.g., from *Lyngbya majuscula*) or macroalgae (e.g., *Hinksia Sordida*) or other  
124 cyanobacteria (e.g., *Synechococcus*), all reported around Australia, can be ruled out. Blooms of  
125 *Synechococcus* rarely form algae scums, and their reflectance peaks around 550 nm (Soja-Wozniak  
126 et al., 2018; Cannizzaro et al., 2019) as opposed to ~600 nm. Likewise, the reflectance spectral  
127 shapes of *Lyngbya majuscula* mats are relatively smooth in the visible wavelengths (Roelfsema et  
128 al., 2006), dramatically different from those of *Trichodesmium* scums. Finally, *Hinksia Sordida* is  
129 a benthic brown macroalgae (Sanderson, 1997) that is unlikely to have pigment composition  
130 similar to that of *Trichodesmium* to result in similar spectra shapes as shown in Figs. S2e and S3b.  
131 From all spectroscopy results, the greenish features in the VIIRS FRGB images must be due to  
132 *Trichodesmium* scums. The distinctive pigment features (Fig. S3b) suggest that the *Trichodesmium*  
133 cells are not dead (for otherwise they would not show these pigment features) but actively fixing  
134 nitrogen and carbon, as demonstrated in a field experiment in the Arabian Sea (Capone et al., 1998).

135 Assisted with the spectroscopy analysis as shown in Figs. S2e and S3b, the visually identified  
136 algae features in the VIIRS images are delineated using a combination of manual outlining and  
137 objective segmentation (Hu et al., 2023). The manual outlining is used to determine where in the  
138 image to apply the segmentation technique, while the segmentation is based on the spatial gradient

139 of  $R_{rc}$ . A sample result is shown in Fig. S2c. Such images are used as the “ground truth” to train  
140 and validate the deep-learning model.

141 Step 2. Develop and validate a Res-UNet deep-learning model to detect algae pixels from VIIRS  
142 images

143 The deep residual U-Net (Res-UNet) model is a kind of segmentation deep learning method which  
144 was proposed by Zhang et al. (2018) to extract the road from remote sensing images. Afterwards,  
145 it has been widely used and applied to other fields, such as automatic segmentation of floating raft  
146 aquaculture, extraction of urban buildings, and so on (Gao et al., 2022; Wen et al., 2019). Recent  
147 applications to multi-band ocean color data suggest its robustness in extracting macroalgae image  
148 features from MODIS in the Atlantic Ocean (Hu et al., 2023). Here, we developed a deep learning  
149 (DL) model from the Res-UNet architecture to extract *Trichodesmium* image features, and then  
150 quantify *Trichodesmium* density using a pixel unmixing scheme. The model works as follows:

151 **Model training.** In this study, the inputs of the Res-UNet model consist of 4 VIIRS bands and  
152 an alternative floating algae index (AFAI), all normalized according to their dynamic ranges.  
153 Here AFAI is defined as (Qi et al., 2016):

$$154 \quad AFAI = R_{\lambda_2} - \left[ R_{\lambda_1} + \frac{\lambda_2 - \lambda_1}{\lambda_3 - \lambda_2} \times (R_{\lambda_3} - R_{\lambda_1}) \right], \quad (2)$$

155 where the three VIIRS wavelengths are  $\lambda_1 = 671$  nm,  $\lambda_2 = 745$  nm, and  $\lambda_3 = 862$  nm.

156 The normalization of  $R_{rc}$  was performed as

$$157 \quad nR_{rc} = [\log(R_{rc}) - \log(R_{rc}^{(Min)})] / [\log(R_{rc}^{(Max)}) - \log(R_{rc}^{(Min)})], \quad (3)$$

158 where  $R_{rc}^{(Min)}$  and  $R_{rc}^{(Max)}$  are 0.0025 and 0.3, respectively, for  $R_{rc}$  data of all 4 bands at 486, 551,  
159 671, and 862 nm. Likewise, AFAI was normalized as:

$$160 \quad nAFAI = (AFAI - AFAI_{min}) / (AFAI_{max} - AFAI_{min}) \quad (4)$$

161 where  $AFAI_{min} = -0.005$ ,  $AFAI_{max} = 0.02$ . Through the normalization,  $R_{rc}$  and AFAI were scaled  
162 to floating point values in the range of 0.0–1.0.

163 The above process is repeated over a total of 10,652 sub-images, each being  $128 \times 128$  in size and  
164 representing images collected under different observation conditions (e.g., sun glint, thin clouds,  
165 large viewing angles, shallow water). The resulting 10,625 images are called “labeled images” and

166 used as the “ground truth” images to train and validate the deep-learning model, as described below.  
167 Once fully trained, the application of the model only requires images with 5 channels (4  $R_{rc}$  bands,  
168 1 AFAI) as the input, with the classified algae pixels as the output.

169 **Model validation.** The performance of the Res-UNet model was evaluated by comparing the  
170 model output with the labeled “ground truth” images that were not used in the model training.  
171 Figs. S4 and S5 show sample model outputs, where the classified algae pixels are shown in the  
172 last row as white. These classified pixels were compared with those from the labeled images to  
173 determine the following statistical measures:

$$174 \quad Precision = \frac{TP}{TP+FP} \times 100\%, \quad (5)$$

$$175 \quad Recall = \frac{TP}{TP+FN} \times 100\%, \quad (6)$$

$$176 \quad F1 = \frac{2 \times Precision \times Recall}{Precision + Recall} \times 100\%, \quad (7)$$

177 where TP, FP, and FN stand for true positives, false positives, and false negatives, respectively.  
178 F1 is the overall accuracy measure of the classification results after accounting for both false  
179 positives and false negatives. Here, TP and FP were calculated after accounting for subpixel algae  
180 coverage (see below). The evaluation results are presented in Table S2. Note that these evaluations  
181 are not based on *in situ* measurements but based on carefully prepared “ground truth” images,  
182 therefore can be regarded as a measure of consistency between “ground truth” and the model.

183 The DL model was also evaluated qualitatively using *in situ* data collected by the Integrated  
184 Marine Observing System (IMOS) program (Eriksen et al., 2019). Because of the difference in the  
185 sampling methods (i.e., *Trichodesmium* scums are detected in this study, but *Trichodesmium* cells  
186 in the water column were sampled from fixed locations in the IMOS program), it is difficult to  
187 have a point-to-point comparison. This is also why McKinna (2010) used “ships-of-opportunity  
188 sightings of dense *Trichodesmium* surface aggregations substantial in spatial extent, preferably in  
189 the order of ~10–100 m” to validate satellite observations of surface scums. For this reason, the  
190 IMOS *in situ* data were used to evaluate the presence/absence detection by the DL model.  
191 Specifically, from the IMOS program (Davis et al., 2020), high abundance of *Trichodesmium* was  
192 reported at 5 of the 7 long-term monitoring stations, and these are cases with the DL model showed  
193 frequent *Trichodesmium* scums (Fig. 1a). At the 2 stations (“Kangaroo Island” and “Maria Island”)

194 to the south of Australia where no *Trichodesmium* was observed from the IMOS program, the DL  
195 model did not show any *Trichodesmium* scums either.

196 There are different methods to detect *Trichodesmium* scums using satellite observations (see  
197 review by McKinna (2015)), such as those based on the floating algae index (FAI, Hu et al., 2010),  
198 maximum chlorophyll index (MCI, Blondeau-Patissier et al., 2018), or classification based on  
199 several spectral bands with thresholds (McKinna et al., 2011). While the objective of this study is  
200 not to provide a comprehensive evaluation of different methods in detecting *Trichodesmium* scums,  
201 comparison of these different methods over sample images showed consistency, as shown in Fig.  
202 S6. In this example, the same VIIRS images as in Fig. S2 is used for illustration. Similar spatial  
203 patterns were found between the AFAI and MCI images, both showing more *Trichodesmium* (Figs.  
204 S6b & S6c) than from the classification method (Fig. S6d) because the presence/absence detection  
205 in the latter method is sensitive to the selected threshold. However, VIIRS does not have the 709-  
206 nm band, making the MCI algorithm not applicable. Furthermore, the classification method only  
207 detects the presence of *Trichodesmium* scum without quantifying the subpixel % coverage (see  
208 below). The DL model used in this study was able to improve the performance of AFAI to avoid  
209 false-positive detections over shallow water and thin clouds (Figs. S4 and S5). This is why the DL  
210 model was used in this study. The advantage of a similar DL model in detecting *Sargassum*  
211 macroalgae has been fully detailed in Hu et al. (2023).

212 Step 3. Quantify *Trichodesmium* areal density at the pixel level

213 *Trichodesmium* scums are very patchy, and they rarely cover a kilometer-scale pixel. Therefore,  
214 for all classified algae pixels, a simple unmixing model was used to determine the subpixel  
215 coverage (or areal density), expressed as  $\chi$  (0–100%) (Qi and Hu, 2021). The unmixing was based  
216 on the pixel's AFAI value, using the following equation:

$$217 \quad AFAI^P = \chi AFAI^A + (1-\chi) AFAI^W \quad (8)$$

218 Here,  $AFAI^P$  represents the pixel's AFAI value, and  $AFAI^A$  and  $AFAI^W$  represent the AFAI values  
219 of the algae endmember and water endmember, determined to be 0.127 and  $-0.0005$ , respectively,  
220 from *in situ* *Trichodesmium* and water reflectance (McKinna et al., 2011) resampled for VIIRS  
221 bands. Note that small errors in these endmember values can lead to similar errors in the estimated

222  $\chi$  value. But these errors are systematic across all algae pixels and all images, thus will not impact  
223 either the spatial distribution patterns or the temporal changing patterns.

224 Step 4. Derive *Trichodesmium* areal density maps

225 After pixel unmixing, *Trichodesmium* areal density maps were derived following the same  
226 approach outlined in Qi et al. (2016). Briefly, the study region was divided into 9-km grids. For  
227 each grid, the mean *Trichodesmium* density (in %) during a given period (e.g., month) was  
228 calculated as:

$$229 \quad f = \frac{1}{N_t} \sum_{i=0}^{N_t} \chi_i, \quad (9)$$

230 where  $N_t$  is the number of valid pixels from all images during that period in that grid. In this process,  
231 cloud and sun glint pixels are masked as invalid, using the following criteria:

$$232 \quad \text{mask} = \text{where}(R_{rc}(486) > a \& R_{rc}(551) > a \& R_{rc}(671) > a). \quad (10)$$

233 Here, the threshold  $a$  of 0.04 is higher than the NASA default threshold of  $R_{rc}(865)$  at 0.027 to  
234 mask clouds. This is because the AFAI index is tolerant to thin clouds, and the use of a higher  
235 threshold would lead to more valid pixels to apply the Res-UNet model.

236 Such derived *Trichodesmium* density maps for the climatological months of 2012–2021 are  
237 presented in Fig. S7, and for the calendar years are presented in Fig. S8. The total areal coverage  
238 of *Trichodesmium* (km<sup>2</sup>) during a month or a year is the integration of  $f$  over all grids for that  
239 period. Likewise, for the entire study period of 2012–2021, the mean density map is presented in  
240 Fig. 1a, where the total areal coverage is estimated from Fig. 1a using the same integration method.  
241 The cumulative footprint of *Trichodesmium* is defined as the waters (grids) where  $f$  is  $> 0.001\%$ ,  
242 representing waters where *Trichodesmium* scums can be found regardless of their density. The size  
243 of the footprint (in km<sup>2</sup>) is much higher than the *Trichodesmium* areal coverage because  $f$  was used  
244 to estimate the latter. Here, a threshold of 0.001% was selected because (1)  $> 95\%$  of the non-zero  
245 grids have their  $f$  values  $> 0.001\%$  and (2) the non-zero grids with  $f < 0.001\%$  were discarded in  
246 order to account for possible noise due to occasional false positive detection.

247 Using this method, the mean annual areal coverage of *Trichodesmium* between 2012 and 2021 is  
248 presented in Fig. S9, together with other environmental variables (see below).

249

250

#### 251 **4. Quantify *Trichodesmium*'s water and atmospheric environments**

##### 252 **Water environment**

253 The water environment of *Trichodesmium* was characterized by nutrient availability, temperature,  
254 and Chl-a. Of these, the distribution of N/P ratio shows the general nutrient availability (Fig. 3a).  
255 SST and Chl-a corresponding to each algae pixel were extracted from the daily images, with  
256 statistics (i.e., histograms) presented in Figs. 1b & 1d, respectively. Furthermore, from each daily  
257 image, SST and Chl-a were extracted from the *Trichodesmium* niche area (i.e., the multi-year  
258 cumulative footprint in Fig. 1a), and these data served as the “background” to determine whether  
259 *Trichodesmium* prefers a certain SST or Chl-a range over the background environment. Such  
260 statistics are also presented in Figs. 1b and 1d, respectively.

261 Similarly, monthly SST and Chl-a data were extracted from the multi-year cumulative  
262 *Trichodesmium* footprint (Fig. 1a) to calculate climatology monthly means. These data were  
263 overlaid over the seasonal changes of *Trichodesmium* to determine whether they are synchronized  
264 in time (Fig. 2a), and presented in Fig. 3 to show their spatial distributions.

##### 265 **Atmospheric environment**

266 Similar to SST and Chl-a, wind speed from each algae pixel and from the *Trichodesmium* niche  
267 area was pulled from daily images, with statistics presented in Fig. 1c and climatological  
268 distributions presented in Fig. 3e.

269 Monthly dust and black carbon (BC) data were extracted from the multi-year cumulative  
270 *Trichodesmium* footprint (Fig. 1a) to calculate climatological monthly means. These data were  
271 overlaid over the seasonal changes of *Trichodesmium* to determine whether they are synchronized  
272 in time (Fig. 2a). The monthly dust and BC data were also overlaid over the monthly time series  
273 of *Trichodesmium* (Fig. 2b) and annual time series of *Trichodesmium* (Fig. S9) for the same  
274 purpose.

275 To examine whether there is a temporal correspondence between water column Chl-a and other  
276 variables, their climatological monthly means over the *Trichodesmium* niche area (Fig. 1a) are  
277 presented in Fig. S10. To test whether the inter-annual patterns of *Trichodesmium* areal coverage  
278 can be explained by large scale climate events such as El Niño and La Niña, the Multivariate ENSO

279 Index (MEI) was plotted together with *Trichodesmium* monthly anomalies (i.e., difference  
280 between calendar month and climatological month) in the areal coverage (Fig. S11). To verify  
281 whether changes in SST or MLD could be a reason of the observed increases in *Trichodesmium*  
282 and Chl-a after the 2019–2020 bushfire event (Fig. 4), monthly anomalies of SST and MLD in the  
283 water area where BC was found unusually high (outlined in rectangle in Fig. 4b) are presented in  
284 Fig. S12.

## 285 5. Statistical method

### 286 The Mann-Kendall test

287 To test the long-term trend of *Trichodesmium* blooms, we used the Mann-Kendall test through an  
288 open-source python package (Hussain & Mahmud, 2019, <https://pypi.org/project/pymannkendall/>)  
289 to obtain the trend and *p*-values.

### 290 291 Multiple linear regression

292 An analysis of multiple linear regression model (Chatterjee and Hadi, 1986) was used to test the  
293 influence factors associated with *Trichodesmium* bloom changes. The format of multiple linear  
294 regression model in this study is:

$$295 \log(Y) = a_0 + a_1x_1 + a_2x_2 + a_3x_1x_2, \quad (11)$$

296 where *Y* is the area of *Trichodesmium* blooms estimated from VIIRS images, and *x*<sub>1</sub> and *x*<sub>2</sub> are dust  
297 and BC density from M2T1NXAER model.

298 The analysis was applied to both climatological months means (Fig. S13a) and long-term monthly  
299 means (Fig. S13b) for the entire study region as well as to individual grids (Fig. S13c).

## 300 301 Reference

- 302  
303 Bell, P.R.F. (2021). Analysis of satellite imagery using a simple algorithm supports evidence that  
304 *Trichodesmium* supplies a significant new nitrogen load to the GBR lagoon. *Ambio*, 50,  
305 1200-1210  
306 Cannizzaro, J., C. Hu, K. L. Carder, C. R. Kelble, N. Melo, E. M. Johns, G. A. Vargo, and C. A.  
307 Heil (2013). On the accuracy of SeaWiFS ocean color data products on the West Florida  
308 Shelf. *J. Coastal Res.*, 29(6), 1257--1272. DOI: [http://dx.doi.org/10.2112/JCOASTRES-D-](http://dx.doi.org/10.2112/JCOASTRES-D-12-00223.1)  
309 12-00223.1.  
310 Cannizzaro, J.P., Barnes, B.B., Hu, C., Corcoran, A.A., Hubbard, K.A., Muhlbach, E., Sharp,  
311 W.C., Brand, L.E. and Kelble, C.R., 2019. Remote detection of cyanobacteria blooms in an

312 optically shallow subtropical lagoonal estuary using MODIS data. *Remote Sensing of*  
313 *Environment*, 231, p.111227. <https://doi.org/10.1016/j.rse.2019.111227>.

314 Capone, D. G., A. Subramaniam, J. P. Montoya, M. Voss, C. Humborg, A. M. Johansen, R. L.  
315 Siefert, and E. J. Carpenter (1998). An extensive bloom of the N<sub>2</sub> fixing cyanobacterium  
316 *Trichodesmium* in the Eastern Arabian Sea. *Mar. Ecol. Prog. Ser.* 172:281-292.

317 Chatterjee, S., & Hadi, A. S. (1986). Influential observations, high leverage points, and outliers  
318 in linear regression. *Statistical science*, 379-393.

319 Chin, T. M., Vazquez-Cuervo, J., & Armstrong, E. M. (2017). A multi-scale high-resolution  
320 analysis of global sea surface temperature. *Remote Sensing of Environment*, 200, 154-169.

321 Eriksen, R. S., Davies, C. H., Bonham, P., Coman, F. E., Edgar, S., McEnulty, F. R., McLeod,  
322 D., Miller, M. J., Rochester, W., & Slotwinski, A. (2019). Australia's long-term plankton  
323 observations: the integrated marine observing system national reference station network.  
324 *Front. in Mar. Sci.*, 161.

325 Gao, L., Wang, C., Liu, K., Chen, S., Dong, G., & Su, H. (2022). Extraction of Floating Raft  
326 Aquaculture Areas from Sentinel-1 SAR Images by a Dense Residual U-Net Model with  
327 Pre-Trained Resnet34 as the Encoder. *Remote Sensing*, 14(13), 3003.  
328 <https://www.mdpi.com/2072-4292/14/13/3003>

329 Hu, C. (2022). Hyperspectral reflectance spectra of floating matters derived from Hyperspectral  
330 Imager for the Coastal Ocean (HICO) observations. *Earth Syst. Sci. Data*, 14, 1183–1192,  
331 <https://doi.org/10.5194/essd-14-1183-2022>.

332 Hu, C., J. Cannizzaro, K. L. Carder, F. E. Muller-Karger, and R. Hardy (2010). Remote detection  
333 of *Trichodesmium* blooms in optically complex coastal waters: Examples with MODIS full-  
334 spectral data. *Remote Sens. Environ.*, 114:2048-2058.

335 Hu, C., S. Zhang, B. B. Barnes, Y. Xie, M. Wang, J. P. Cannizzaro, and D. C. English (2023).  
336 Mapping and quantifying pelagic Sargassum in the Atlantic Ocean using multi-band  
337 medium-resolution satellite data and deep learning. *Remote Sens. Environ.*, 113515,  
338 <https://doi.org/10.1016/j.rse.2023.113515>.

339 Hussain, M., & Mahmud, I. (2019). pyMannKendall: a python package for non parametric Mann  
340 Kendall family of trend tests. *Journal of Open Source Software*, 4(39), 1556.

341 IOCCG (2019). Uncertainties in Ocean Colour Remote Sensing. Mélin F. (ed.), IOCCG Report  
342 Series, No. 18, International Ocean Colour Coordinating Group, Dartmouth, Canada.  
343 <http://dx.doi.org/10.25607/OBP-696>.

344 McKinna, L. I. W. (2010). Optical detection and quantification of *Trichodesmium* spp. within the  
345 Great Barrier Reef, PhD thesis, James Cook University, Australia, 312 pp.,  
346 <https://researchonline.jcu.edu.au/15643/> (last access: 8 March 2022).

347 McKinna, L. I. W., Furnas, M. J., & Ridd, P. V. (2011). A simple, binary classification algorithm  
348 for the detection of *Trichodesmium* spp. within the Great Barrier Reef using MODIS  
349 imagery. *Limnology and Oceanography: Methods*, 9(2), 50-66.  
350 <https://doi.org/https://doi.org/10.4319/lom.2011.9.50>

351 Mikelsons, M., & Wang, M. (2018). Interactive online maps make satellite ocean data accessible.  
352 *Eos*, 99.

353 Qi, L., & Hu, C. (2021). To what extent can *Ulva* and *Sargassum* be detected and separated in  
354 satellite imagery? *Harmful Algae*, 103, 102001.  
355 <https://doi.org/https://doi.org/10.1016/j.hal.2021.102001>

356 Qi, L., Hu, C., Mikelsons, K., Wang, M., Lance, V., Sun, S., Barnes, B. B., Zhao, J., & Van der  
357 Zande, D. (2020). In search of floating algae and other organisms in global oceans and lakes.



358 *Remote Sensing of Environment*, 239, 111659.  
359 <https://doi.org/https://doi.org/10.1016/j.rse.2020.111659>  
360 Qi, L., Hu, C., Xing, Q., & Shang, S. (2016). Long-term trend of *Ulva prolifera* blooms in the  
361 western Yellow Sea. *Harmful Algae*, 58, 35-44. <https://doi.org/10.1016/j.hal.2016.07.004>  
362 Roelfsema, C. M., S. R. Phinn, W. C. Dennison, A. G. Dekker, and V. E. Brando (2006).  
363 Monitoring toxic cyanobacteria *Lyngbya majuscula* (Gomont) in Moreton Bay, Australia by  
364 integrating satellite image data and field mapping. *Harmful Algae*, 5:46-56.  
365 doi:10.1016/j.hal.2005.05.001.  
366 Sanderson, J. C. (1997). Subtidal macroalgal assemblages in temperate Australian coastal waters,  
367 Australia: State of the Environment Technical Paper Series (Estuaries and the Sea),  
368 Department of the Environment, Canberra. ([https://www.researchgate.net/profile/J-](https://www.researchgate.net/profile/J-Sanderson/publication/236688368_Subtidal_Macroalgal_Assemblages_in_Temperate_Australian_Coastal_Water/links/0deec532ba8270e29e000000/Subtidal-Macroalgal-Assemblages-in-Temperate-Australian-Coastal-Water.pdf)  
369 [Sanderson/publication/236688368\\_Subtidal\\_Macroalgal\\_Assemblages\\_in\\_Temperate\\_Austr](https://www.researchgate.net/profile/J-Sanderson/publication/236688368_Subtidal_Macroalgal_Assemblages_in_Temperate_Australian_Coastal_Water/links/0deec532ba8270e29e000000/Subtidal-Macroalgal-Assemblages-in-Temperate-Australian-Coastal-Water.pdf)  
370 [alian\\_Coastal\\_Water/links/0deec532ba8270e29e000000/Subtidal-Macroalgal-Assemblages-](https://www.researchgate.net/profile/J-Sanderson/publication/236688368_Subtidal_Macroalgal_Assemblages_in_Temperate_Australian_Coastal_Water/links/0deec532ba8270e29e000000/Subtidal-Macroalgal-Assemblages-in-Temperate-Australian-Coastal-Water.pdf)  
371 [in-Temperate-Australian-Coastal-Water.pdf](https://www.researchgate.net/profile/J-Sanderson/publication/236688368_Subtidal_Macroalgal_Assemblages_in_Temperate_Australian_Coastal_Water/links/0deec532ba8270e29e000000/Subtidal-Macroalgal-Assemblages-in-Temperate-Australian-Coastal-Water.pdf), accessed 5/29/2023).  
372 Soja-Wozniak, M., M. Darecki, B. Wojtasiewicz, and K. Bradtke (2018). Laboratory  
373 measurements of remote sensing reflectance of selected phytoplankton species from the  
374 Baltic Sea. *Oceologia*, 60:86-96. <http://dx.doi.org/10.1016/j.oceano.2017.08.001>  
375 Wen, Q., Jiang, K., Wang, W., Liu, Q., Guo, Q., Li, L., & Wang, P. (2019). Automatic Building  
376 Extraction from Google Earth Images under Complex Backgrounds Based on Deep Instance  
377 Segmentation Network. *Sensors*, 19(2), 333. <https://www.mdpi.com/1424-8220/19/2/333>  
378 Zhang, Z., Liu, Q., & Wang, Y. (2018). Road extraction by deep residual u-net. *IEEE*  
379 *Geoscience and Remote Sensing Letters*, 15(5), 749-753.  
380  
381

382 Table S1. Summary of previous studies on remote sensing of *Trichodesmium* blooms (surface  
383 scums) around Australia (Fig. S1).

Study	Coverage	Duration	Sensor & Method
Subramaniam & Carpenter (1994)	21°S, 118.5°E	Sample images: Nov. 1980	CZCS, classification from $L_t$
Capone et al. (1997)	20.5°S–19°S 117°E–120.5°E	Sample images	CZCS, classification from $L_t$
Gower et al., 2008	24.5°S–18.5°S 148°E–156°E	Sample images: Aug. 2006	MERIS, MCI from $L_t$
McKinna et al., 2011	24°S–10°S 142°E–153°E	Sample images: Jan. 2005; Oct. 2007	MODIS, classification from $R_{rs}$
Blondeau-Patissier et al. (2014)	19.5°S–15°S, 145°E–147.5°E 13°S–9°S, 130°E–133°E	Time series: 2002–2012	MERIS, MCI from $L_t$
Blondeau-Patissier et al. (2018)	26°S–9°S 142°E–155°E	Time series: 2002–2012	MERIS, MCI from $L_t$
Bell (2021)	19°S, 147.35°E 20.4°S, 149°E 22.7°S, 151.3°E	Sample images: Aug. 2011; Jan. 2005; Jul. 2008	MODIS, classification from $R_{rs}$

384

385

386 Table S2. Accuracy of the Res-UNet model to detect and estimate *Trichodesmium* surface  
387 coverage from VIIRS satellite imagery. The corresponding images are shown in Fig. S4 and Fig.  
388 S5, respectively.

Date of image	<i>Tricho</i> weighted area (km <sup>2</sup> )	TP (km <sup>2</sup> )	FP (km <sup>2</sup> )	FN (km <sup>2</sup> )	Precision	Recall	F1
09/12/2013	1062.0	978.2	20.0	83.8	98.0%	92.1%	95.0%
10/29/2019	357.0	337.8	10.2	19.2	97.1%	94.6%	95.8%

389 \*TP is true positives, FP is false positives, and FN is false negatives. Precision, Recall, and F1 were calculated using  
390 Eqs. (5)–(7).

391

392

393

394

395

396

397

398

399

400

401

402

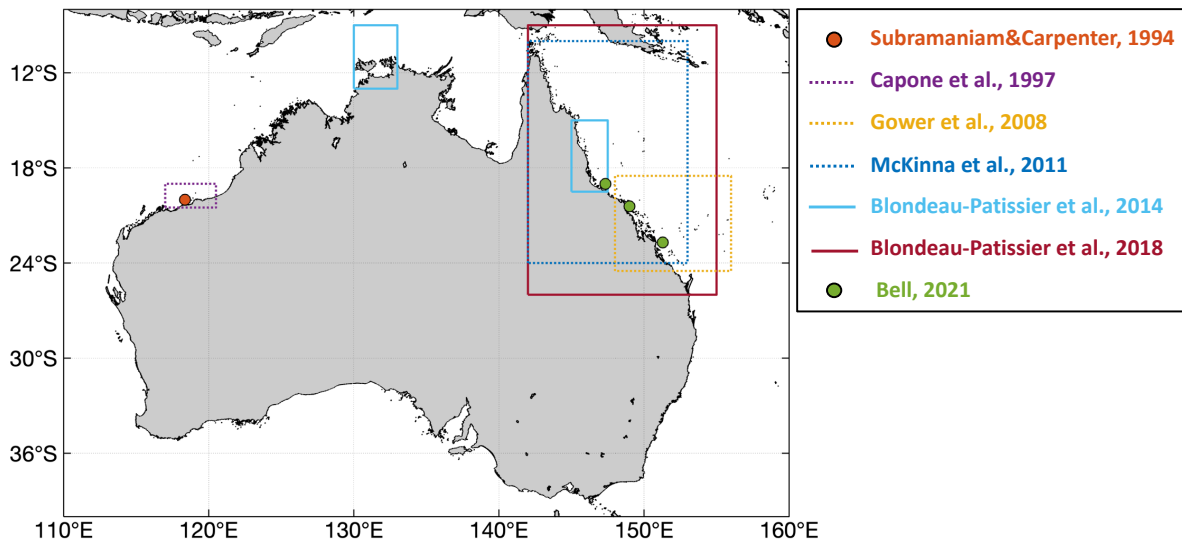
403

404  
405  
406  
407

Table S3. Monthly mean areal coverage (in km<sup>2</sup>) of *Trichodesmium* scums around Australia from VIIRS observations between 2012 and 2021. Bold font indicates the peak month of the year.

Month	2012	2013	2014	2015	2016	2017	2018	2019	2020	2021
Jan.	393.2	609.6	290.9	256.5	238.1	221.7	196.1	209.5	185.4	162.7
Feb.	194.9	541.9	<b>458.5</b>	<b>508.5</b>	225.9	274.8	233.5	464.4	138.9	260.9
Mar.	87.5	445.7	275.2	438.9	110.6	77.4	168.3	359.0	94.9	179.7
Apr.	75.4	174.1	140.6	114.9	41.2	26.7	99.8	56.6	4.8	91.1
May	9.8	21.6	29.2	58.6	87.9	12.8	10.8	27.2	13.3	30.8
Jun.	41.9	22.8	44.5	10.2	61.3	11.5	25.0	25.0	41.1	30.6
Jul.	37.6	83.3	54.1	25.8	58.1	69.4	78.4	75.3	194.4	109.8
Aug.	143.2	324.4	64.8	77.7	234.2	187.9	271.2	110.9	185.4	195.6
Sep.	647.5	731.4	366.3	214.5	401.4	491.5	444.7	995.8	507.7	389.6
Oct.	583.7	635.4	437.8	478.3	327.4	<b>607.5</b>	<b>998.8</b>	<b>1283.3</b>	<b>563.1</b>	<b>647.6</b>
Nov.	314.4	<b>1019.8</b>	284.9	148.6	<b>497.5</b>	262.6	342.5	548.1	407.0	613.2
Dec.	<b>793.8</b>	608.7	287.9	150.8	151.6	304.2	184.0	347.2	274.4	154.9

408  
409  
410  
411  
412  
413  
414  
415  
416  
417  
418  
419  
420



422 Fig. S1. Map showing study regions of earlier remote sensing works (rectangles and dots), with  
 423 references annotated in the map legend (also see Table S1). The map covers 40°S–8°S and 110°E–  
 424 160°E, which is the study region of the current work. The solid rectangle shows the long-term time  
 425 series study, while the dashed rectangles and dots show case studies. No *Trichodesmium* scums  
 426 were found between 40°S and 44°S (including waters around Tasmania), and this area is therefore  
 427 not included in the map.

428

429

430

431  
 432  
 433  
 434  
 435  
 436  
 437  
 438  
 439  
 440  
 441  
 442  
 443  
 444  
 445  
 446  
 447  
 448  
 449  
 450  
 451  
 452  
 453  
 454  
 455  
 456  
 457  
 458  
 459  
 460  
 461  
 462  
 463  
 464  
 465  
 466  
 467  
 468  
 469  
 470  
 471  
 472  
 473  
 474  
 475

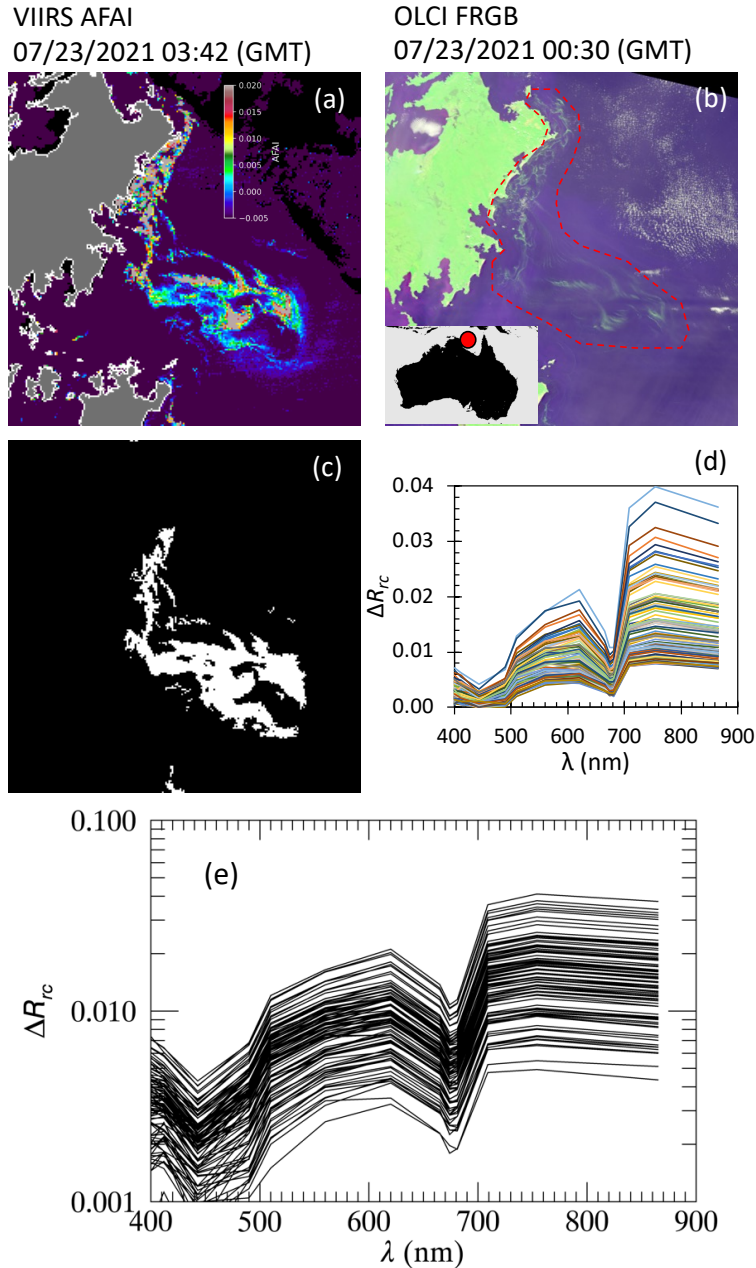


Fig. S2. Examples showing the input images for the Res-UNet model for (a) VIIRS AFAI image and (b) OLCI FRGB image on 23 July 2021 over an area of 12–14°S, 136–138°E. Color bar in (a) shows the AFAI values for each pixel, and greenish in red dash polygon in (b) indicates the *Trichodesmium* bloom area. The insert map in (b) with the red circle shows the location of the images taken at (13°S, 137°E); (c) white pixels were labeled as *Trichodesmium* as input for the Res-UNet model training and validation; (d) OLCI reflectance spectra from randomly selected algae-scum pixels from the outlined area, which show typical *Trichodesmium* spectral shapes (Qi et al., 2020). For clarify, the spectra of 100 randomly selected algae-scum pixels are plotted in log scale in (e), which appear parallel to each other, indicating the same algae type (i.e., *Trichodesmium*). The same validation has been performed using randomly selected OLCI and VIIRS image pairs, with results near identical to those of (e).

476  
477  
478  
479  
480  
481  
482  
483  
484  
485  
486  
487  
488  
489  
490  
491  
492  
493  
494  
495  
496  
497  
498  
499  
500  
501  
502  
503  
504  
505  
506  
507  
508  
509  
510  
511  
512  
513  
514  
515  
516  
517  
518  
519  
520

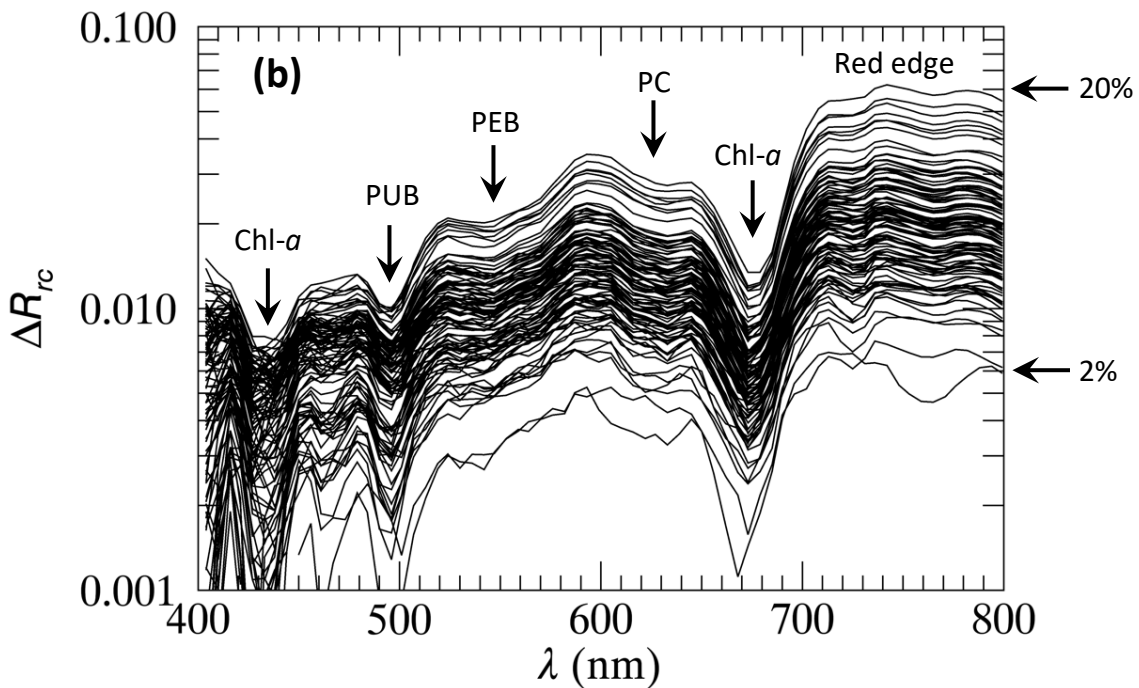
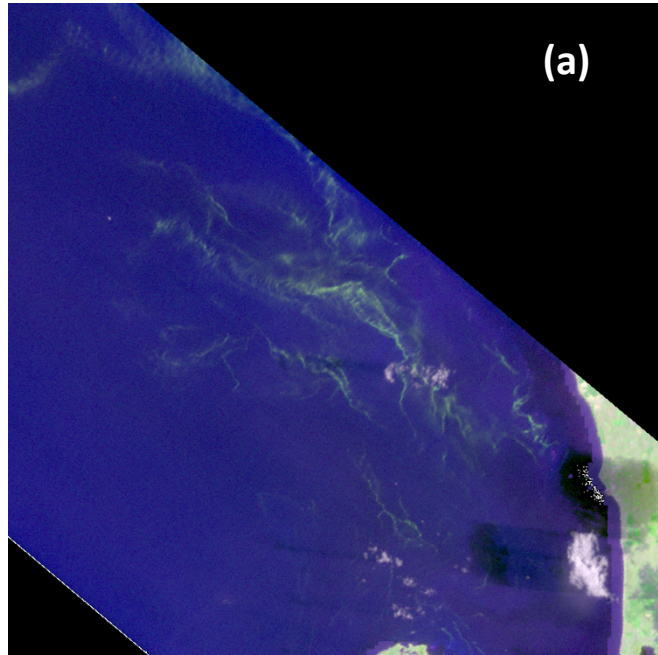
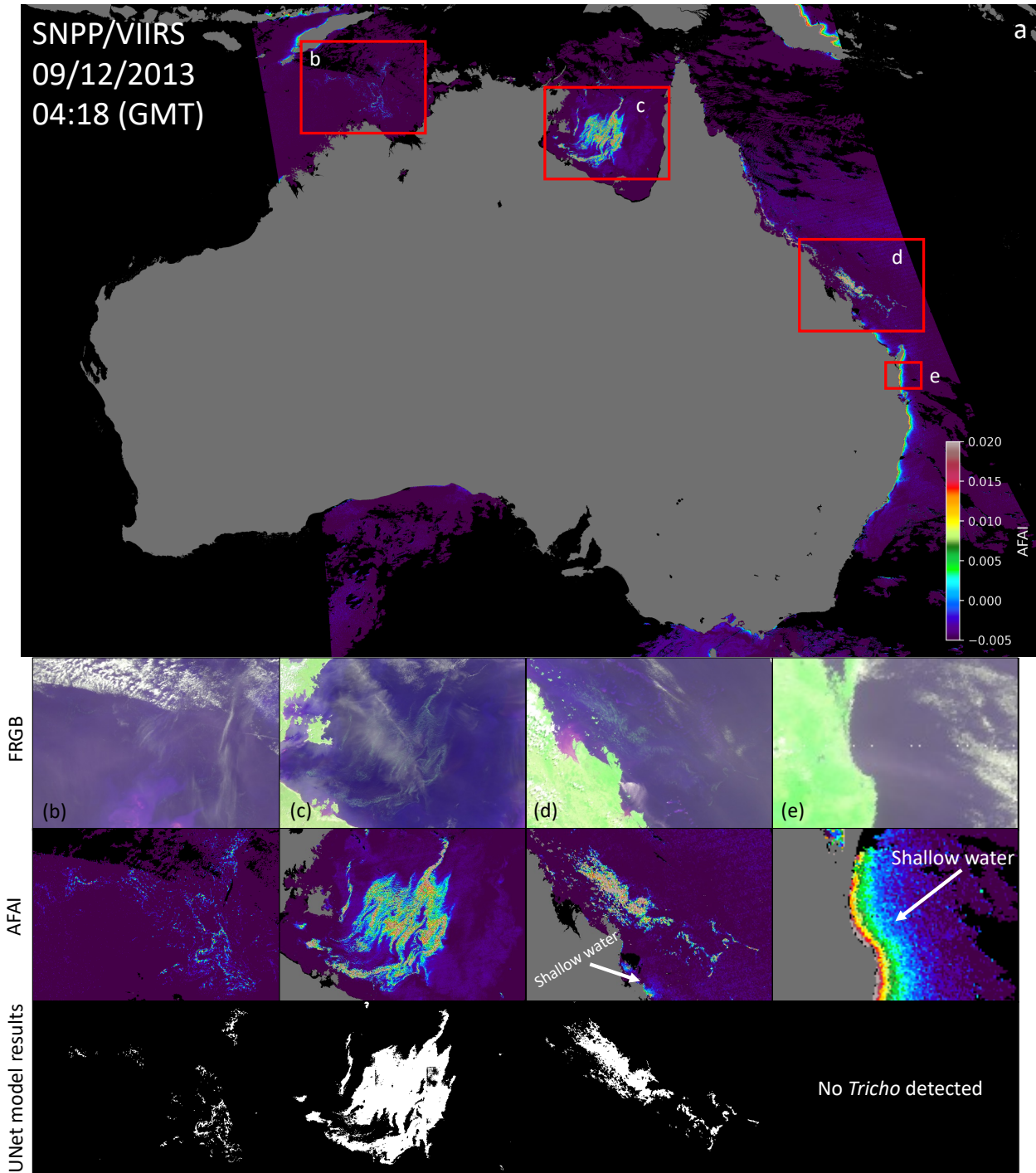
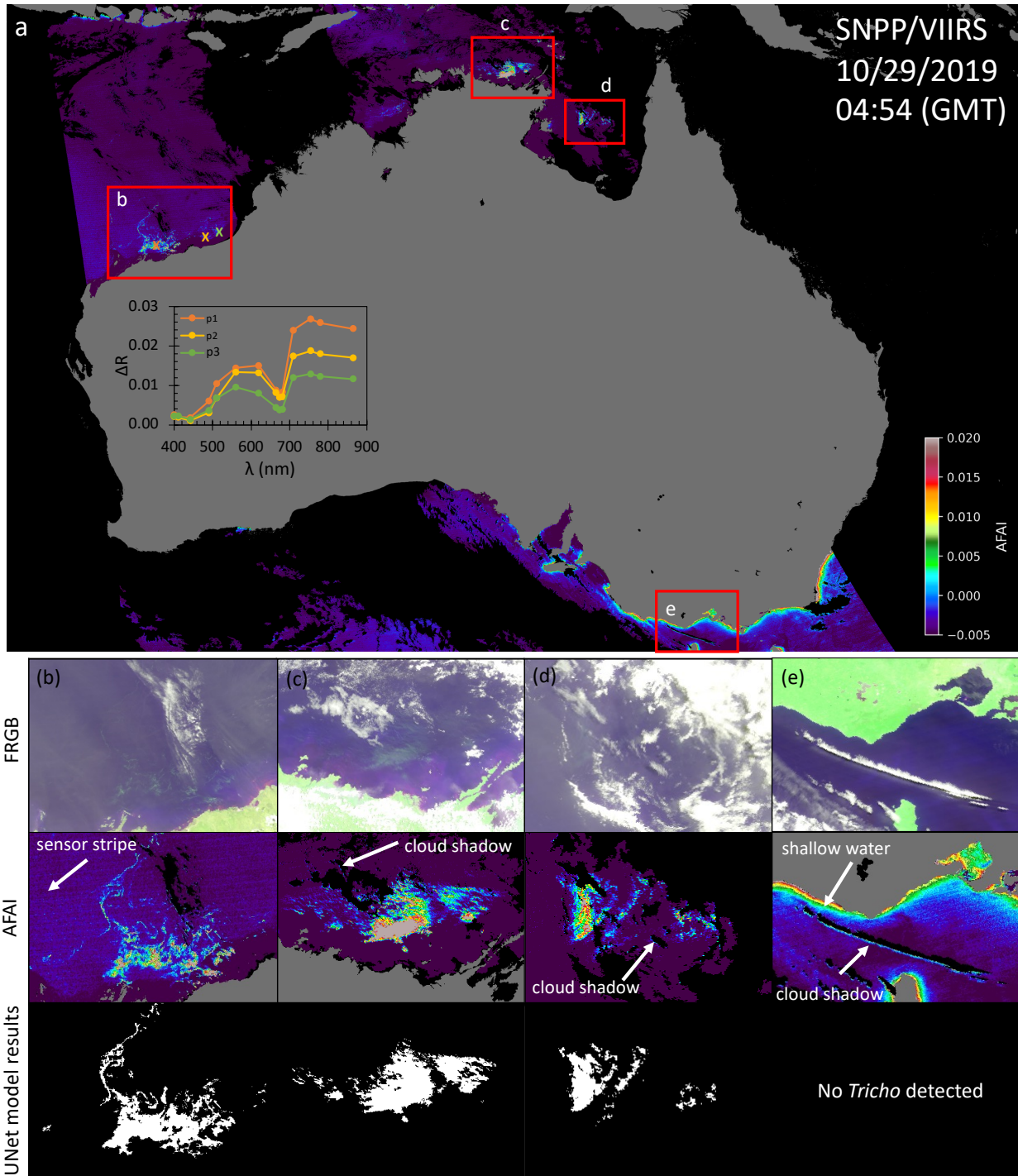


Fig. S3. (a) HICO FRGB image collected on 9 December 2012 off the southwest coast of Australia (31.3°S–32°S, 115.1°E–115.8°E) showing algae scums (greenish image features); (b) Reflectance spectra of 100 randomly selected pixels from the algae scums, with spectral features annotated, i.e., PUB: phycourobilin; PEB: phycoerythrobilin, PC: phycocyanin. These reflectance spectral shapes are nearly identical (i.e., parallel to each other in log scale), indicating the same algae type. The changes in magnitudes indicate different algae density ( $\chi$ ) within a pixel, annotated to the right.



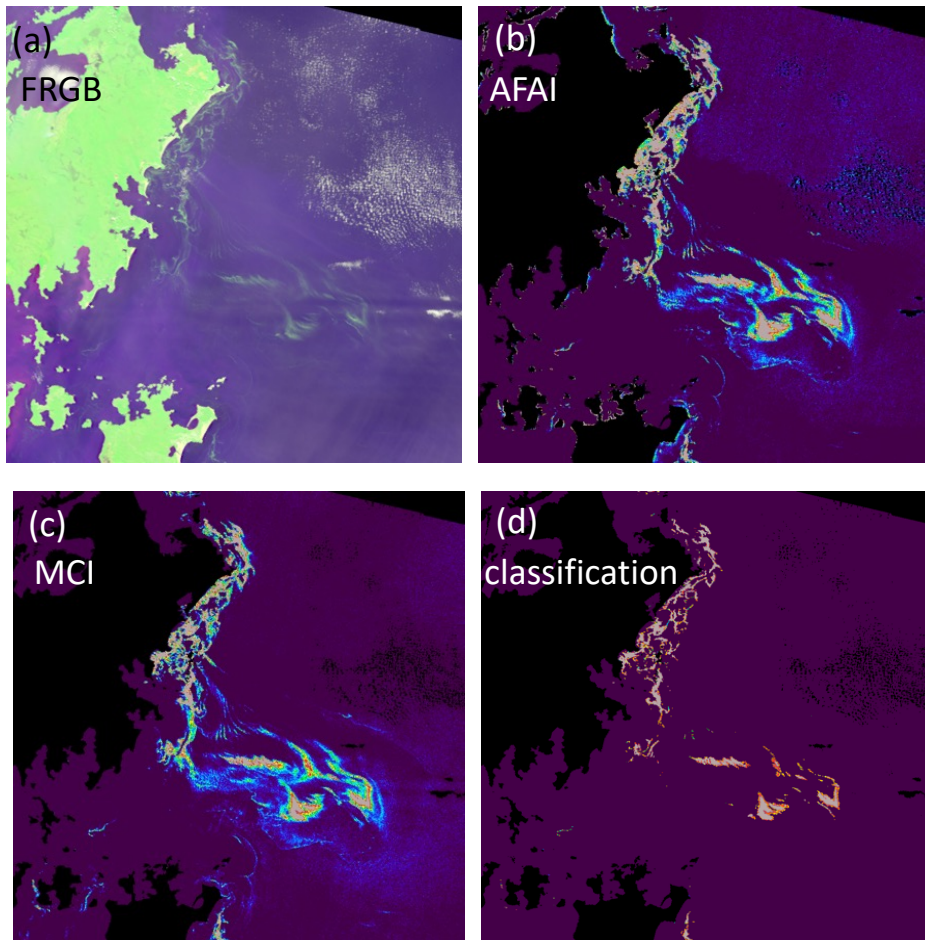
521 Fig. S4. Examples showing extraction of *Trichodesmium* surface scum using the Res-UNet model  
 522 for (a) VIIRS AFAI image on 12 September 2013, where 4 small regions are shown in (b)–(e),  
 523 respectively, with their corresponding FRGB images, AFAI images, and Res-UNet model results  
 524 presented separately. In the AFAI images, black represents clouds, sun glint, extremely turbid  
 525 water, or no satellite coverage, while white arrows indicate high AFAI values caused by shallow  
 526 water rather than by *Trichodesmium*. The Res-UNet model correctly identified these pixels as non-  
 527 *Trichodesmium*, as illustrated in the bottom row.



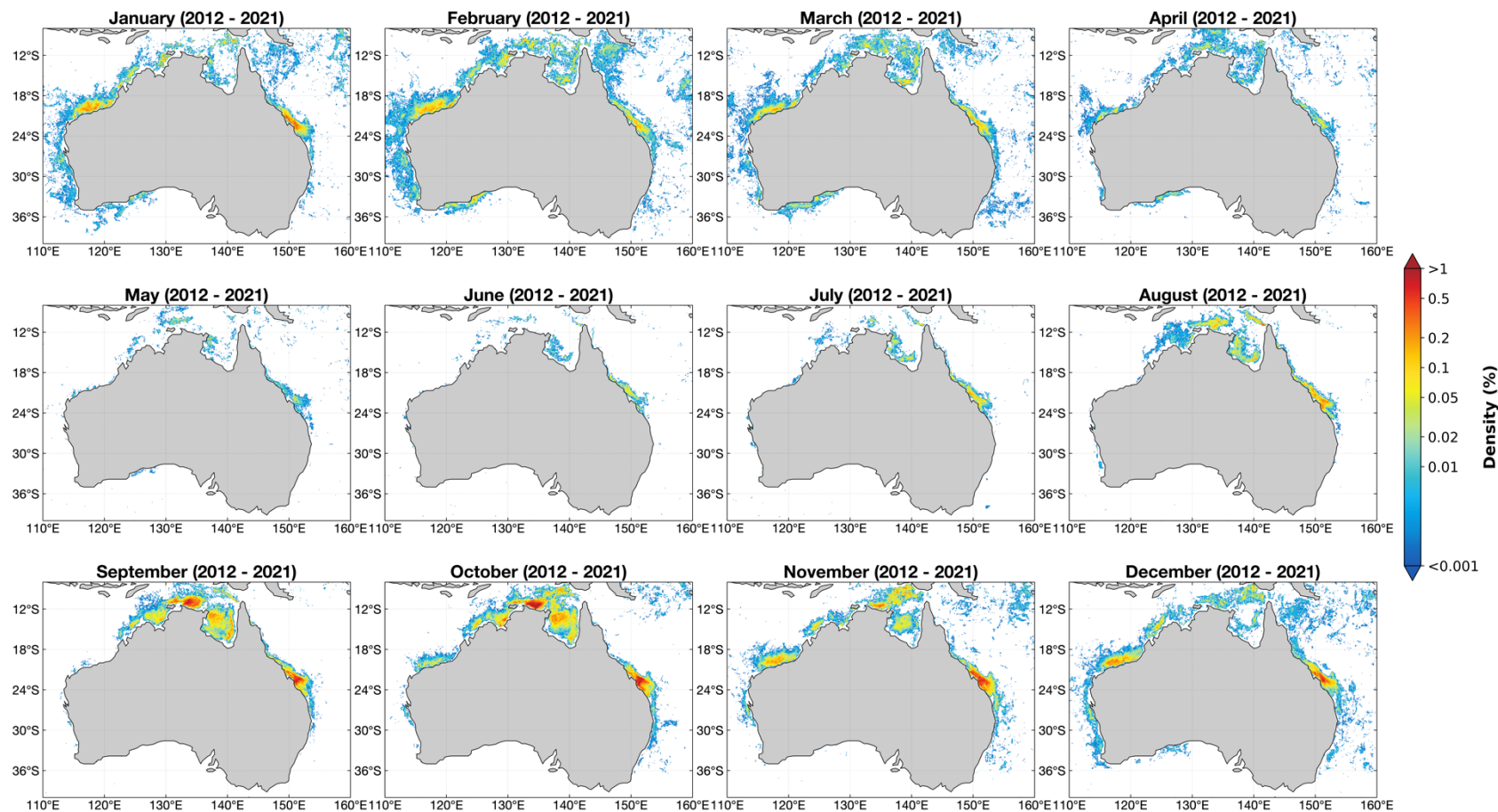
528 Fig. S5. Examples showing extraction of *Trichodesmium* surface scum using the Res-UNet model  
 529 for (a) VIIRS AFAI image on 29 October 2019, where 4 small regions are shown in (b)–(e),  
 530 respectively, with their corresponding FRGB images, AFAI images, and Res-UNet model results  
 531 presented separately. In the AFAI images, black represents clouds, sun glint, extremely turbid  
 532 water, or no satellite coverage, while white arrows indicate high AFAI values caused by shallow  
 533 water, striping noise, and cloud shadow. The Res-UNet model correctly identified these pixels as  
 534 non-*Trichodesmium*, as illustrated in the bottom row.



535  
536  
537  
538  
539  
540  
541  
542  
543  
544  
545  
546  
547  
548  
549  
550  
551  
552  
553  
554  
555  
556  
557  
558  
559  
560

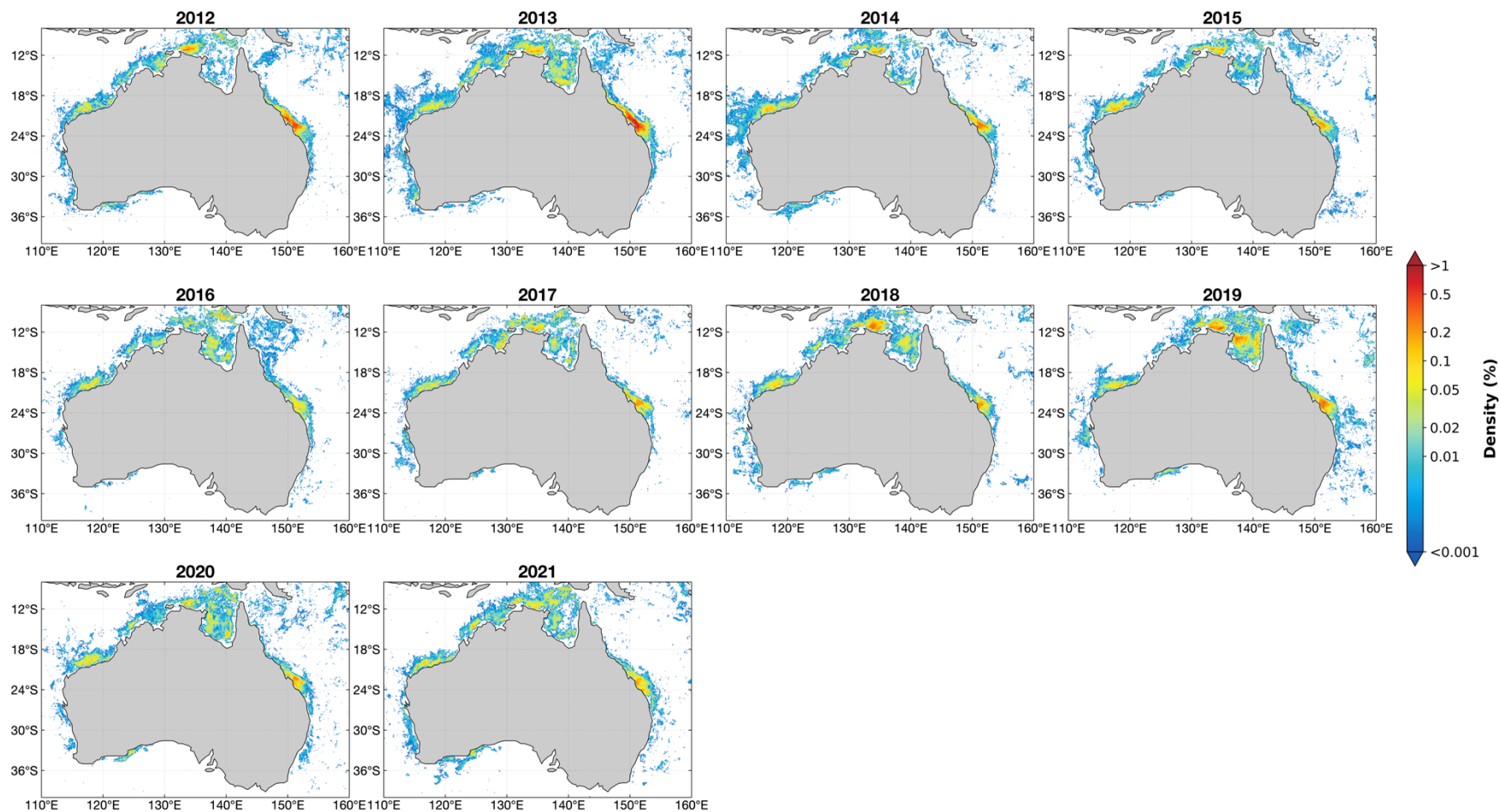


561 Fig. S6. Comparison between different methods in detecting *Trichodesmium* scums from OLCI  
562 images. (a) FRGB image showing surface features. This is the same image as in Fig. S2; (b) The  
563 corresponding AFAI image; (c) The corresponding MCI image (Blondeau-Patissier et al., 2018);  
564 the corresponding classification results (McKinna et al., 2011). The DL model in this study is  
565 based on AFAI and other spectral bands.



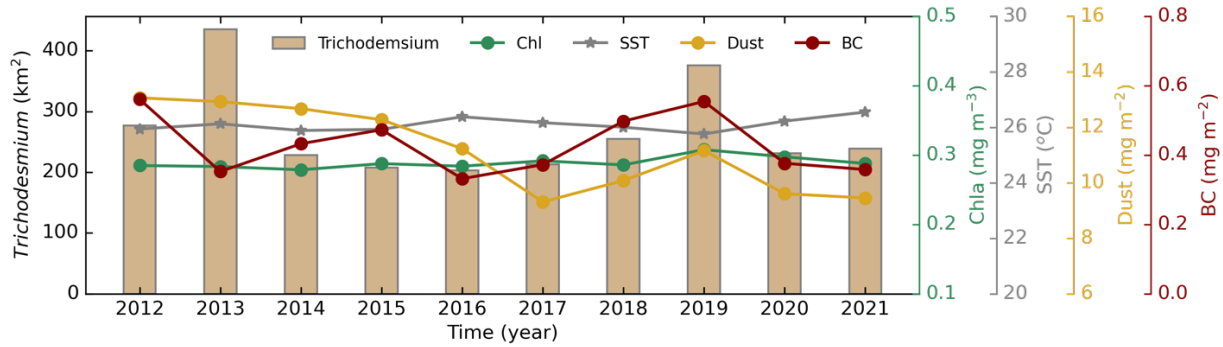
566 Fig. S7. Cumulative footprint and surface coverage density of *Trichodesmium* in each climatological month of 2012–2021. The density  
 567 is expressed as mean % coverage in a given location.

568  
 569  
 570  
 571

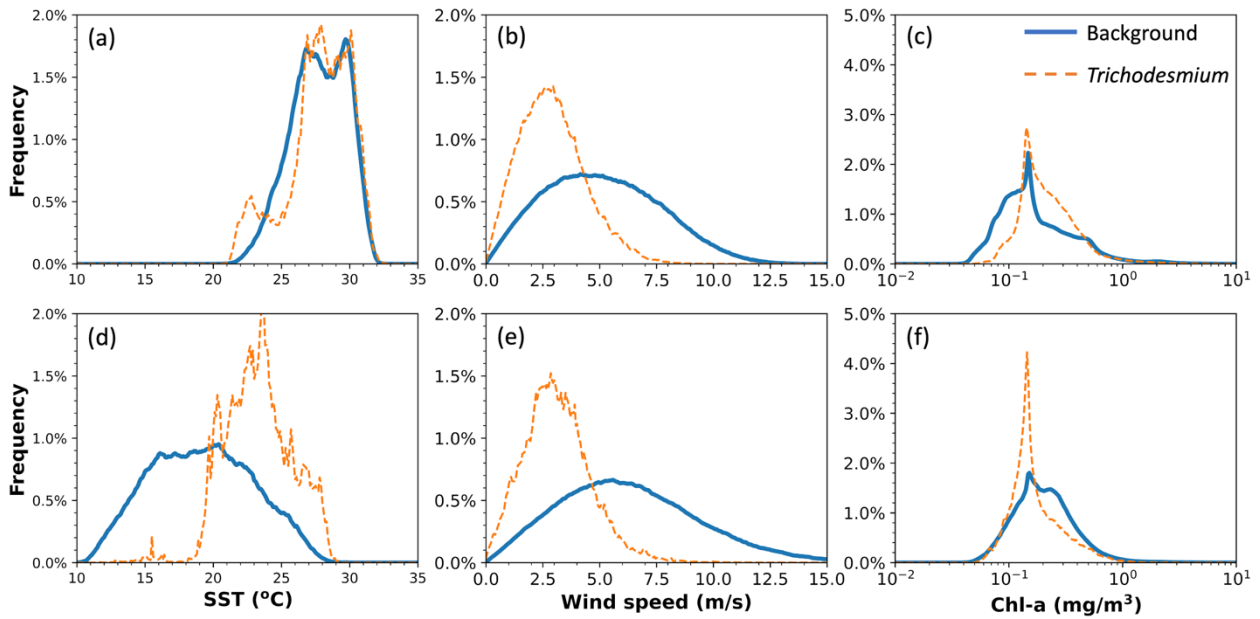


572  
573  
574  
575

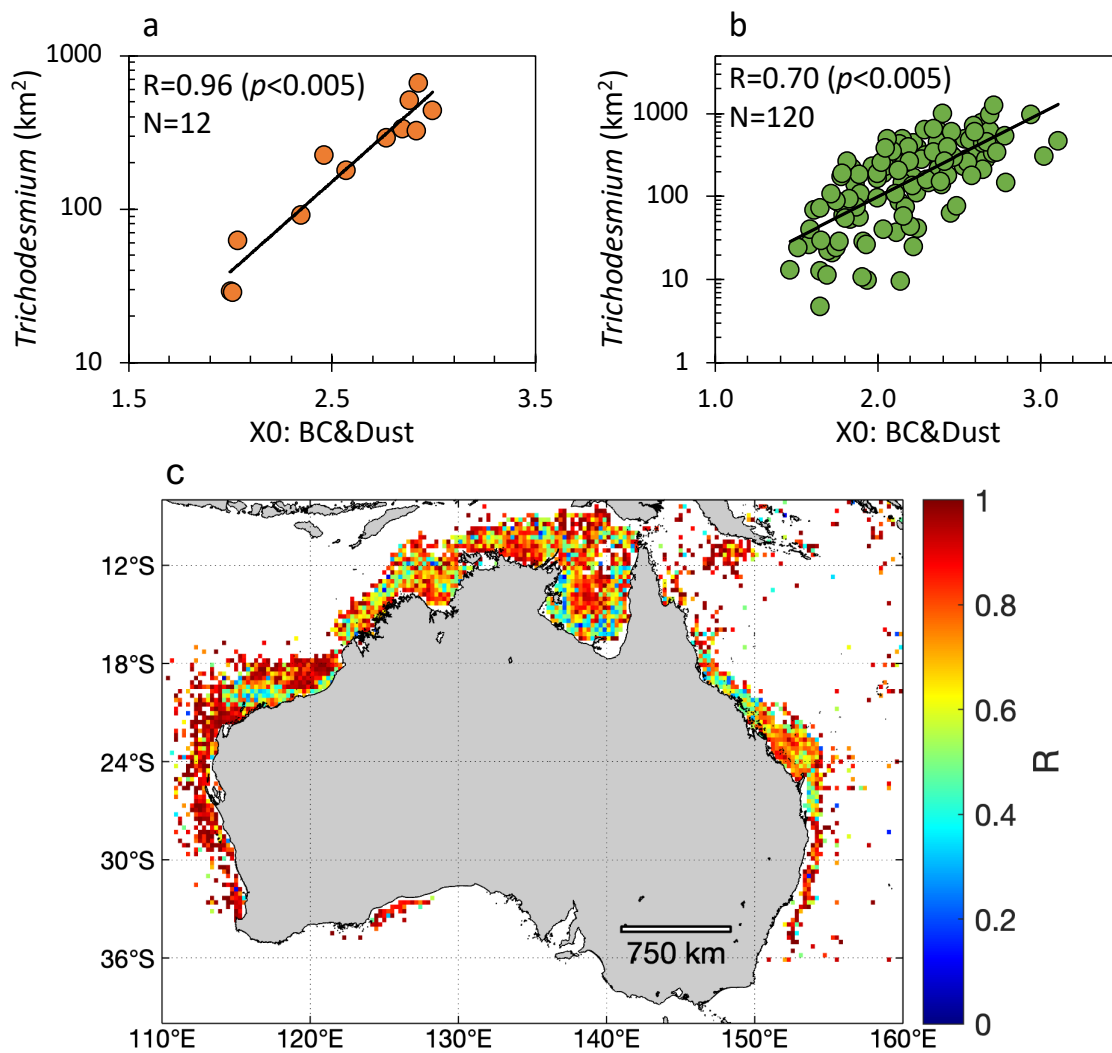
Fig. S8. Cumulative footprint and surface coverage density of *Trichodesmium* in each calendar year of 2012–2021, calculated from monthly maps during each year. The density is expressed as mean % cover in a given location.



576  
 577 Fig. S9. Annual mean area of *Trichodesmium* scums (km<sup>2</sup>) around Australia, together with the  
 578 annual mean Chl-a, SST, BC, and dust.  
 579  
 580  
 581



582  
 583 Fig. S10. Similar to Figs. 1b-d, but the analysis was over (a) – (c) tropical/subtropical waters (north  
 584 of 23.45°S) and (d) – (f) temperate waters (south of 23.45°S). Here, “Background” water refers to  
 585 waters in the *Tricho*-niche area, while “*Trichodesmium*” water refers to locations of  
 586 *Trichodesmium* occurrence. See Fig. 1 caption for more details.  
 587  
 588  
 589  
 590



592

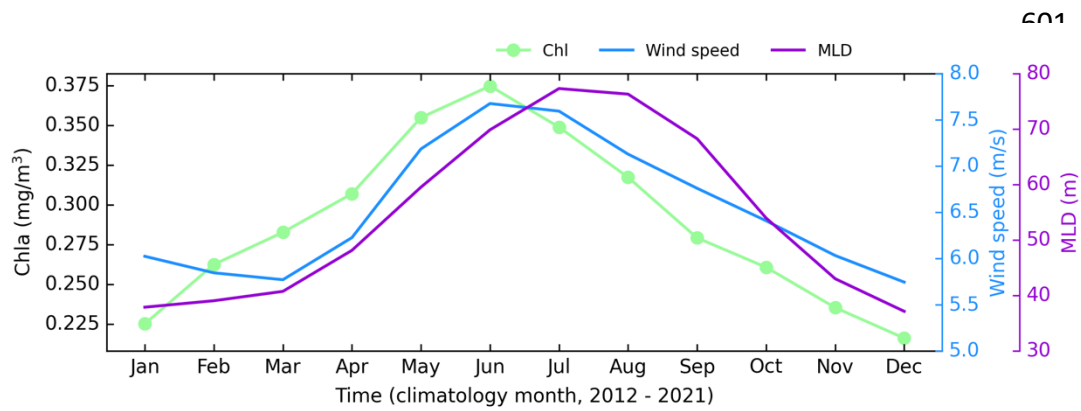
593

594

595 Fig. S11. Multi-variate analysis between BC, dust, and *Trichodesmium* on their seasonality. (a)596 For climatology months ( $X_0 = 5.43 \times \text{BC} + 0.35 \times \text{Dust} - 0.41 \times \text{BC} \times \text{Dust} + 1.91$ ); (b) For calendar597 months ( $X_0 = 3.46 \times \text{BC} + 0.16 \times \text{Dust} - 0.21 \times \text{BC} \times \text{Dust} - 0.03$ ); (c) Spatial distributions of the598 correlation after binning all data to 50-km grids. The unit of  $X_0$  in (a) and (b) is  $\text{mg m}^{-2}$ .

599

600



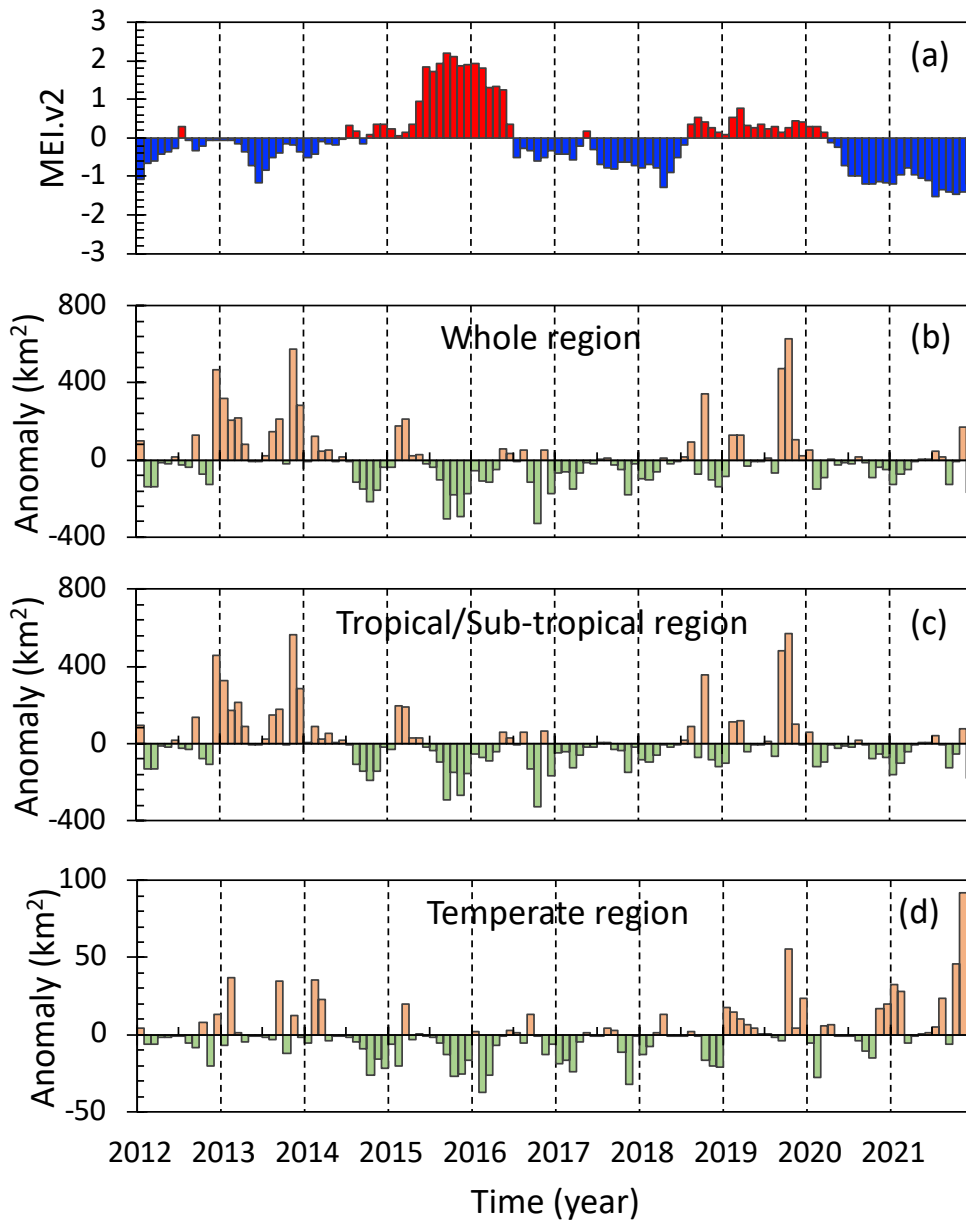
612

613 Fig. S12. Seasonality of Chl-a, Wind speed, and mixed-layer depth (MLD) derived from the  
614 *Trichodesmium* niche area (Fig. 1a) between 2012 and 2021.

615

616

617



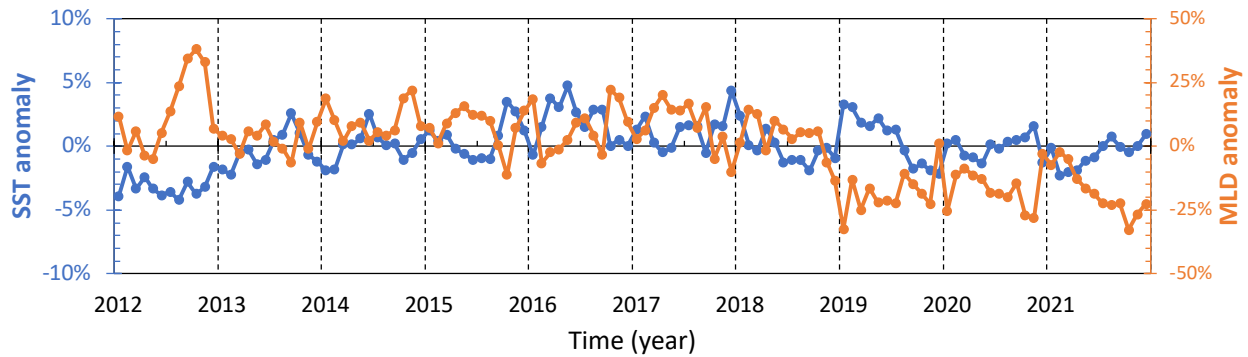
653

654 Fig. S13. (a) Multivariate ENSO Index (MEI, version2 data product) between 2012 and 2021  
 655 (data obtained from NOAA, <https://psl.noaa.gov/enso/mei/>), with red for El Niño phase and blue  
 656 for La Niña phase; (b–d) monthly mean *Trichodesmium* coverage anomaly around Australia  
 657 derived from VIIRS over the entire region, tropical/sub-tropical region (north of 23.45°S), and  
 658 temperate region (south of 23.45°S), respectively.

659

660

661



662 Fig. S14. Monthly anomalies of SST and MLD in a region off the southeast Australia (outlined in  
663 rectangle in Fig. 4b) where BC was much higher than usual in late 2019 due to the bushfire event.  
664 SST does not show anomalies higher than interannual variability, and negative MLD anomalies  
665 (i.e., shallower mixed layer) started at the beginning of 2019 (i.e., not synchronized with other  
666 changes shown in Fig. 4c). The shallower mixed layer also suggests lower amount of nutrients  
667 from the deep ocean is available for *Trichodesmium* and other phytoplankton.